8-11-2014 12:00 AM

Intensity Based Non-rigid Registration of 3D Whole Mouse Optical and MR Image Volumes

Jacqueline Kathleen Harris, *The University of Western Ontario*

INTENSITY BASED NON-RIGID REGISTRATION OF 3D WHOLE MOUSE OPTICAL AND MR IMAGE VOLUMES

(Thesis format: Integrated-Article)

by

Jacqueline, <u>Harris</u>

Schulich School of Medicine and Dentistry

Graduate Program in Medical Biophysics

A thesis submitted in partial fulfillment
of the requirements for the degree of
Master of Science

The School of Graduate and Postdoctoral Studies
The University of Western Ontario
London, Ontario, Canada

August 2014

Abstract

Novel magnetic resonance (MR) imaging techniques can be validated using accurate co-registration with histology. Whole-animal histological sections allow for simultaneous analysis of multiple tissues, and may also aid in registration by providing contextual information and structural support to tissues which if isolated from the body would be difficult to register.

This thesis explores the feasibility of co-registration between whole mouse histology with 3D MR images using an intermediate optical image volume acquired during tissue sectioning. Of the two transformations required for this approach, 3D co-registration of MR and optical images is more challenging to perform due to changes in contrast, slice orientation, and resolution between these modalities. Here, an automated non-rigid registration technique utilizing mutual information is proposed to accurately register 3D whole mouse optical and MR images as a first step towards automated registration of histology. Validation of this technique was accomplished through calculation of post-registration target registration error.

Keywords: Magnetic Resonance Imaging (MRI), Histology, Optical Imaging, Registration, Whole Mouse Imaging, Mutual Information

Co-Authorship

Contributions of work from other individuals include cryo-sectioning, optical image acquisition and histology collection by Amanda Hamilton. MR image acquisition was assisted by Colin McCurdy, Lanette Friesen-Waldner and Kevin Sinclair. Manual registration technique for histology-optical co-registration developed by Eli Gibson along with code for creating 3D optical volumes from 2D block face images.

To my parents for their unwavering love and support

And my sister Stephanie for leading the way

Acknowledgements

Table of Contents

Table of Figures

List of Abbreviations

2D	Two-dimensional
3D	Three-dimensional
CT	Computerized Tomography
DSC	Dice Similarity Coefficient
FLE	Fiducial Localization Error
FOV	Field of View
IDEAL	Iterative Decomposition of Water and Fat with Echo Asymmetry and least Squares Estimation
ITK	Insight Tool Kit
MI	Mutual Information
MMI	Mattes Mutual Information
MR	Magnetic Resonance
MRI	Magnetic Resonance Imaging
MSE	Mean Squared Error
NCC	Normalized Cross Correlation
NIR	Near-infrared
OCT	Optimal Cutting Temperature Media
PD	Proton Density
RF	Radio Frequency
T	Tesla

T1	Longitudinal Relaxation Time.
T1w	T1-weighted
T2	Transverse Relaxation Time
T2w	T2-weighted
TE	Echo Time
TR	Repeat Time
TRE	Target Registration Error

Chapter 1 :

Introduction

1.1 Motivation

The spatial alignment of images can be an important component of image processing for quantitative comparison. The process of aligning images differing in some way but capturing the same object is known as image registration. Specifically, the goal of image registration is to find an optimal transformation, mapping all points from one image to the other. Applications of this can be found in various fields; however, it has proven to be particularly valuable in analysis of medical images.

In medical imaging, the goal of image registration is to find a transformation in which the homologous anatomies of two or more images are aligned. The process of doing this will compensate for superficial differences between the images resulting from changes in patient posture, sensor location and other sources to be removed; enabling more important features of the images to be compared and correlated.

There are a number of sources of variation between images, differences in the sensor, time of acquisition, and the patient being imaged are some examples. Notably, a difference in the mode of image acquisition offers a unique opportunity to combine images depicting different properties of the same anatomy. Examples of this type of registration can be found in numerous medical applications and using a variety of different imaging modalities. However, for this thesis the focus will be specifically on registration between histology and magnetic resonance (MR) images. Comparison of these particular modalities enables validation of novel magnetic resonance imaging (MRI) contrasts using histology, a common clinical diagnostic gold standard.

Generally, approaches to this type of registration focus on a specific organ or tissue as a result of conventional approaches to histological preparation wherein tissues are processed once isolated. Alternatively, processing of whole-animal histological sections can address registration of multiple tissues simultaneously. Also this may enable accurate registration of tissues which significantly deform once isolated from the body.

However, no techniques attempting automated registration of whole mouse MR images and histological sections have been proposed. This study attempts to approach this problem by using an optical image to bridge the gap between these two modalities. As an initial step towards registration of histology and MRI the feasibility of MRI and optical image co-registration is investigated here. This can later be combined with a registration for histological sections and their corresponding optical images. Together, these two registrations will align whole mouse histology and MR images.

1.2 Histology

The field of histology focuses on the examination of microscopic tissue composition and structure. This is accomplished through the collection of tissue samples thin enough to allow the transmission of light, which may be examined under a light microscope. The power of this technique lies in its capability to image at extremely high resolution, allowing direct visualization of tissue architecture, cells and sub cellular structures. This can be of particular use in the study of different disease states, in which microscopic changes to tissues occur. Moreover, the development of a number of histological stains and staining techniques has made histology an invaluable tool in biological research; enabling specific structural and molecular components of the tissue to be highlighted and easily visualized.

Preparation techniques of tissue for histology attempt to create thin sections while maintaining the *in vivo* tissue structure. Although the specifics of any particular preparation may vary to suit the requirements of a given application, there are a few steps that remain consistent in most conventional protocols[1]. The first step is to isolate the tissue of interest for processing. Clinically, this is accomplished by collecting a small sample of tissue, known as a biopsy. In pre-clinical research, animals are euthanized and tissues, as large as an organ, are collected. Once isolated, the tissue is fixed to prevent degradation and then embedded in some sort of medium, such as paraffin wax, which when solidified creates a block. This tissue block is then thinly sectioned using a machine called a microtome which repeatedly shaves away thin layers of tissue from one of the block faces. Specifically in this work a cryo-sectioning protocol was used, in which the tissue is fixed by freezing it once embedded within a gel medium. To maintain the tissues frozen state during sectioning, the microtome is operated within a freezer (figure 1.1). As the tissue is sectioned it may be collected on microscope slides. Once tissue sections have been collected, more specific staining protocols may be employed to achieve the desired contrast.

In many disease states including prostate[2] and breast[3] cancer, as well as liver fibrosis[4], pathological evaluation of histology is the gold standard for disease diagnosis and staging. This remains the case despite continuous efforts in the field of medical imaging to replace it. Largely, the continued stance of histology as the gold standard for diagnosis is its capability to directly image tissue architecture and cellular composition, to which the classifications of many diseases are based. For the most part, non-invasive imaging is

Figure 1.1: CryoViz^{TM} cryo-imaging system used for sectioning and optical imaging of frozen mouse volumes

forced to measure tissue changes on a larger scale (millimeters) in which subtle changes may be less apparent or undetectable.

While providing invaluable information into the structure and composition of tissues, as well as being supported by extensive research linking histological appearance to different disease states, pathological tissue evaluation does suffer from a number of critical limitations. Clinically, histology generally comes in the form of a biopsy, introducing risk to the patient in the form of infection[5, 6]. Additionally, it suffers from sampling error due to the small sample size; potentially missing important structures such as tumors[7] during

sampling or misrepresenting large heterogeneous tissues[8, 9]. Specifically motivating to this thesis however is the limitation histological preparation places on preclinical research. To collect tissue for histological processing animals must be euthanized. In doing this the ability to perform longitudinal studies is severely limited, requiring multiple animals to be euthanized at different time points in order to understand disease progression and response to potential interventions. While this does allow longitudinal investigation, it prevents each animal from being its own control, and as such important subtle findings may be lost due to inter-animal variability. These downfalls contribute to continuing efforts to develop new diagnostic techniques, such as non-invasive imaging, to potentially replace or correlate with histology and improve diagnostic quality.

1.3 Optical Imaging

The term optical imaging describes a wide range of techniques that utilize the visible, ultraviolet and infrared spectra of electromagnetic waves to generate images[10]. These approaches enable non-invasive imaging of the body without the use of ionizing radiation. Because visible light is utilized, full color images can be generated[11] giving soft tissue structures rich contrast. Moreover, the wavelength of these modalities can support acquisition of high resolution images, allowing visualization at the cellular level[12].

Unfortunately, optical imaging like most other imaging modalities does have critical flaws limiting its applications. Probably the most restricting is the limited depth penetration of visible light. Related to its wavelength, optical imaging is generally restricted to investigating structures within a few millimeters of the tissue surface[13].

Figure 1.2: View of exposed tissue block face during cryo-sectioning

As described previously however, standard procedures for histological processing of tissue inherently offer a unique opportunity for optical imaging of internal structures normally too deep below the surface. This can be accomplished during microtoming, where thin layers of tissue are serially shaved away. During this process, structures normally deep below the skin's surface become exposed along the face of the tissue block as seen in figure 1.2. By alternating between imaging and sectioning of the exposed face,

optical imaging techniques can be employed throughout the tissue volume; allowing optical imaging to be exploited in a novel way.

Specifically, this approach can utilize both bright field and fluorescence microscopy throughout the volume of the animal. Using the bright field microscopy, images can be captured at high resolution, with full color. These provide detailed anatomical images rich in contrast over the entire volume. Additionally, by adding different filters fluorescence images of the tissue face can be acquired, enabling the detection of fluorescently labelled cells or molecular components[13, 14].

Compared to histological images however, the optical images acquired in this manner may have an obstructed view of cellular structure despite acquiring images at an adequate resolution. This results from the remaining tissue block that lies below the exposed tissue face. In contrast, histological tissue is sectioned at a thickness which enables transmission of light, allowing a single layer of cells to be imaged clearly without interfering structures in the background. The two imaging modalities can be used in conjunction to address these limitations. Histological sections, which are more difficult to acquire, can be collected sparsely throughout the volume providing samples of detailed cellular structure. These can then be put into 3D context using the corresponding optical images which fit within the series of optical images covering the full tissue volume. Together these imaging techniques can provide a wealth of information. However, their applications remain limited by their extremely invasive nature.

1.4 Magnetic Resonance Imaging

1.4.1 Generating Images

Magnetic resonance imaging (MRI) is a non-invasive medical imaging technique capable of producing detailed anatomical and pathological images. These images are generated by exploiting the magnetic properties of the body. To do this, an individual is placed within a strong external magnetic field. For most clinical scanners this is usually between 0.5 and 3 Tesla (T). Typically MRI is used to image hydrogen atoms (1H) because of their high natural abundance within the body in the form of water and lipids. Hydrogen nuclei within the body possess a polarized axis around which they rotate. In the absence of this strong magnetic field these axes are randomly oriented. Conversely once within the magnetic field of the MRI scanner, the poles of the nuclei will tend to align with this external field.

Additional energy can then be applied in the form of a radio frequency (RF) pulse; which can be tuned to different frequencies. By changing the frequency of the applied RF pulse different nuclei can be exploited. The RF frequency that will affect a given nuclei is dependent upon both the strength of the external magnetic field and the specific type of nuclei. This frequency is known as the Larmor frequency. Once an RF pulse is applied, certain nuclei will absorb this external energy, become excited, and deflect, no longer aligning with the magnetic field. As this happens, the nuclei will begin to precess around the axis of the magnetic field; similar to the wobble of a spinning top. The rate of precession is also equal to the Larmor frequency. Now that the nuclei have a time varying

magnetic component in the transverse plane, their magnetization can be detected. This signal from the displaced nuclei in the transverse plane can be detected as an electromagnetic wave with a frequency equal to the Larmor frequency; and this is used to generate images. These signals can be detected by receive coils that are generally placed directly on the surface of the desired anatomy. Once the RF pulse is removed, the nuclei will begin to realign with the magnetic field.

A third type of magnetic field, known as a gradient, is also used to generate MR images. These are magnetic fields that linearly vary within the main magnetic field causing a spatial variation in field strength along one of the three orthogonal axes. The purpose of these are to spatially encode signals within the body. Without them, signals detected from nuclei in different positions throughout the body would be indistinguishable. The gradients work because both the excitation pulse and detected signal have frequencies dependent upon the strength of the magnetic field. By altering the gradients in all three axes, nuclei can be selectively excited based on their location within the body and detected signals can be spatially encoded. Application of a number of carefully timed RF pulses in series along with the application of gradients is what is known as a pulse sequence.

1.4.2 MRI Contrasts

As previously described, a series of RF pulses can be combined into what is known as a pulse sequence[15]. While there are a number of different pulse sequences available, all have timing parameters TR and TE which can be altered to exploit different properties of the

tissue to generate image contrast. The TR parameter refers to the repetition time, which is the time between excitation RF pulses. TE is the echo time, which is the time between the RF excitation pulse and sampling of the received signal.

Importantly, tissues have a number of characteristic properties from which MR contrast can be derived. The most notable tissue properties that are used to generate contrast are the proton density (PD) and two characteristic timing parameters T_1 and T_2. In PD images, the contrast is related to the number of hydrogen atoms in a particular volume. For example, fluids generally have higher hydrogen content then bone and will appear brighter in PD images.

The T_1 and T_2 timing parameters refer to the time it takes after the RF pulse for atoms to return to equilibrium, and are referred to as relaxation times. Pulse sequences exploiting T_1 and T_2 relaxation times are known as T_1-weighted (T1w) (figure 1.3 A) or T_2-weighted (T2w) (figure 1.3 B) images respectively. The T_1 timing parameter refers to what is known as the spin-lattice relaxation time, which is the time it takes for atoms of a particular tissue to realign with the main magnetic field. These images are often referred to as anatomical scans, producing good contrast between different tissues.

Alternatively, T2w images are often referred to as pathological images producing good contrast of diseased tissues which often accumulate abnormally large amounts of fluid and appear brighter in these images. The T_2 timing parameter is known as the spin-spin

relaxation and is proportional to the time it takes for the transverse magnetization to relax to zero.

In this study we also utilized a less standard pulse sequence known as iterative decomposition of water and fat with echo asymmetry and least squares estimation (IDEAL)[16]. By exploiting the difference between hydrogen atoms in water and lipid molecules, this pulse sequence generates 3 image contrasts simultaneously: a water-only, fat-only and fat fraction image. The water- and fat-only images are essentially inversions of one another. The water-separated image, (figure 1.3 C), depicts regions high in water content more brightly and regions high in lipids more darkly; fat-separated images are the opposite. The fat fraction images are particularly useful as the pixel intensities represent the percentage of lipid in that location. These values can be used to quantify fat content in a particular region, making these images particularly useful in obesity related disease.

One of the main advantages of MRI over other non-invasive imaging modalities is the wide variety of available contrasts. Compared to computerized tomography (CT) imaging for example, where images are always generated based on the same property of the tissue, which is how much different tissues attenuate or absorb X-rays. For this reason, tissues such as bone which are very dense will always appear brighter than most soft tissues in the body regardless of what imaging parameters are changed. Conversely, MRI is able to generate many contrasts by changing pulse sequence timing parameters to exploit

different tissue properties. This allows different tissues to be highlighted by altering the pulse sequence.

While the main imaging contrasts have been briefly explained here, this is in no way an exhaustive list of available contrasts. Extensive work continues to be done in the field of pulse sequence development to generate new contrasts and improve image acquisition strategies. Moreover, much work is still needed to be done in fully understanding the biological implications of novel contrasts in different disease states.
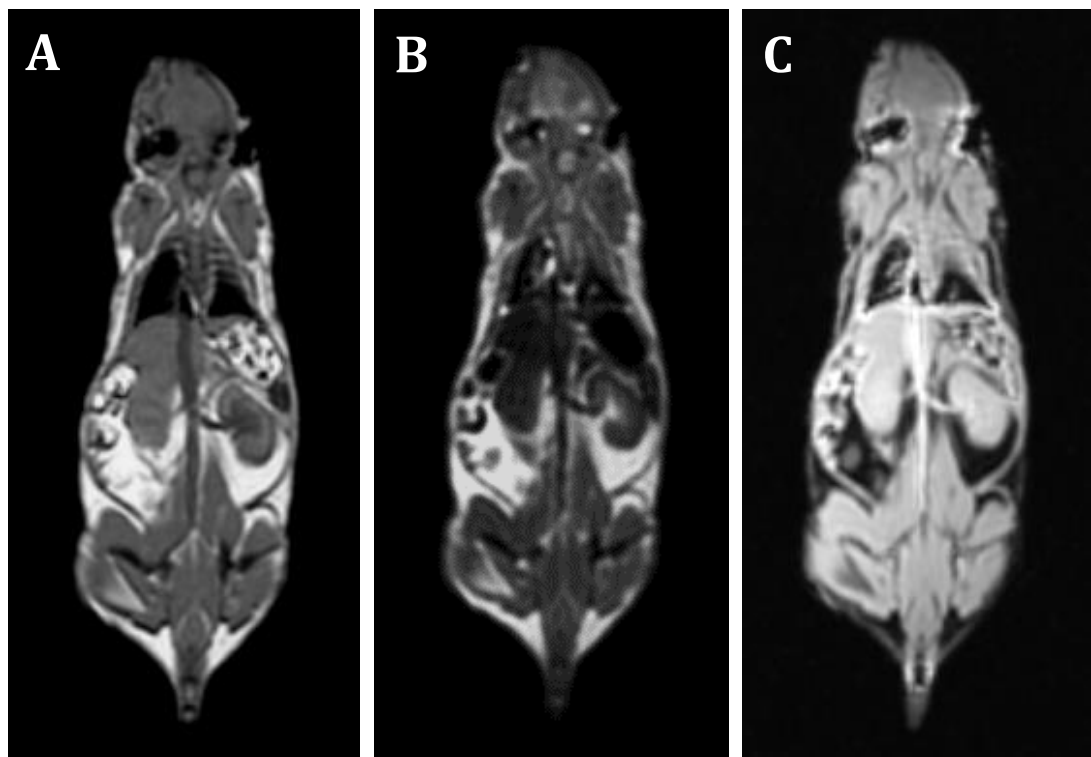
Figure 1.3: MR (A) T1w, (B) T2w, and (C) water-separated IDEAL contrast images of a mouse in the coronal plane.

1.5 MRI-Histology Registration

1.5.1 Motivation

Registration with histology has been recognized as a valuable tool in the development of non-invasive imaging techniques and sought after in many applications. Once registered, histology can be used to understand the microscopic mechanisms behind MRI contrasts. As previously mentioned, histology remains the gold-standard for diagnosis and staging of many diseases, making it in essence a ground truth for non-invasive techniques attempting to image these pathologies. Consequently, registration of histology serves as an important and necessary validation step for novel MRI based diagnostic techniques.

In addition to histology being an important tool for validation of MRI, the two modalities can also be used in conjunction to provide more comprehensive understanding of anatomy. Histology is capable of providing microscopic information about tissue composition and structure, but has a relatively limited field of view. Conversely, MRI typically generates lower resolution images with a much more comprehensive view of the imaged anatomy, providing more information about macroscopic anatomical structure. Together, these two modalities can provide information into macroscopic changes and the underlying mechanisms; potentially giving more meaningful information than either would be able to provide alone.

1.5.2 Problem Description

While desirable, registration of histology with *in vivo* images is a challenging problem. A suitable approach must address a number of discrepancies between the two images. One

difference is the drastic change between contrasts resulting from the different modalities. However, utilization of mutual information based registration techniques have been shown to be quite robust in dealing with this[17] and will be covered more comprehensively in Chapter 2.

The other major obstacle in achieving accurate registration is the tissue deformation that occurs between imaging sessions. This can be broken down into two major sources 1) 3D deformations incurred during tissue excision and embedding steps of histological preparation 2) 2D deformation arising from tissue sectioning. In the latter case, sectioning may also result in tearing or loss of tissue requiring additional processing to recover *in vivo* structure. Both of these sources however can introduce substantial deformations with unique implications on the compensatory approaches.

1.5.3 Approaches

Given the difficulty associated with achieving accurate registration, it is not surprising that many studies investigating non-invasive techniques opt to skip registration in lieu of qualitative comparison based on identifiable anatomical features[18]. While this approach is suitable in some cases, it lacks the accuracy required for quantitative comparison and is often used merely for verification of some quality. As a result of the difficulty associated with this problem, direct registration of histology with *in vivo* images is often avoided. Instead it is common for some sort of intermediate image to be used to bridge the gap between the two modalities; addressing the two sources of tissue deformation in independent steps.

One such approach is to use an *ex vivo* MR image captured of the excised tissue once it has been embedded for sectioning[19, 20]. In doing this, the registration problem can be approached as two easier registrations. The first is co-registration of the *in vivo* and *ex vivo* MR images. While this will have to compensate for substantial deformations resulting from the excision and embedding procedures, the image should have similar contrast, resolution and dimensionality. In an independent step the 2D histological section is registered to the 3D *ex vivo* MR image. This operation will give the histology slice context within the 3D volume and address the change in contrast. However, deformations between the two images should only result from the sectioning procedure making them 2D and theoretically easier to address.

While this approach can greatly aid registration, the problem of finding the ideal placement of the 2D histological section within the *ex vivo* volume can still be challenging. This arises because generally the plane of sectioning will not correspond to the plane of MR imaging; rather an oblique plane through the 3D volume. Theoretically, the volume could intentionally be sectioned to correspond with the MR imaging plane; allowing the histological section to then be registered with the appropriate 2D MR slice. However, even between histological sections from the same specimen there can be considerable variability in the plane of sectioning[21]. Alternatively, MR visible extrinsic markers, or fiducials, can be added to the tissue of interest before *ex vivo* imaging and sectioning[22, 23] to aid in determination of the section position within the volume.

Another commonly used intermediate are optical images captured of the tissue block during sectioning (as previously described in section 1.3) which are also referred to as "block face" images[24-26]. By sectioning the tissue at a consistent thickness and capturing images of the exposed block face at regular intervals, the images can be combined into a 3D volume. Again, this allows registration to be broken down into two steps, one of which is a 3D registration between the *in vivo* MRI and the 3D block face volume. Similar to the use of an *ex vivo* MRI intermediate, this step compensates for deformations incurred during fixation and embedding. However, it will not have the same contrast or resolution, making it slightly more challenging than the previously described approach. The other registration step is a 2D registration of the histological section with the corresponding block face image. While the registration of the two 3D volumes is slightly more complicated as it is now multi-modal, the second registration step becomes considerably easier as the location of the histological section within the optical volume is already known.

Utilizing these approaches, many successful techniques capable of accurately registering histology with *in vivo* MRI volumes have been developed. Despite this progress however, there remain many applications that still have not been addressed. In general, there is not a single approach that is suitable for all tissue types and problems; each scenario has its own unique considerations which will dictate what approach is taken. For this study in particular, an approach utilizing an optical image intermediate will be taken.

Modality:	MRI	Optical	Histology
Voxel Size:	0.6 x 0.6 x 0.7mm	0.02 x 0.02 x 0.2mm	0.5 x 0.5µm
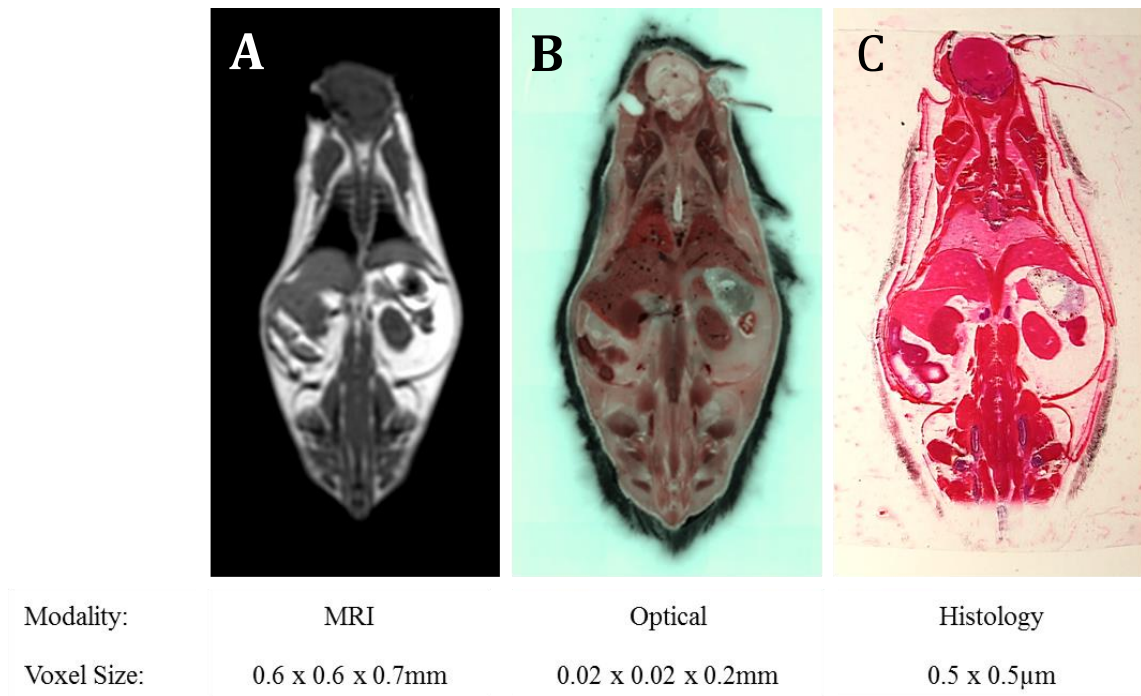
Figure 1.4: Representative (A) T1w MR, (B) optical cryo-section, and (C) histological images with corresponding resolution (given in sagittal x axial x coronal directions respectively for MR and optical images or sagittal x axial for histology).

1.6 Whole Mouse Imaging

1.6.1 Mouse Models

Mice have become an invaluable tool in medical research. Arguably they are imperfect models of human disease however, for ethical and practical reasons they offer many advantages. The use of animal models allows for testing of therapeutic interventions as well as carefully controlled experimental conditions, both of which are not possible in humans. In comparison to other animal models however, a number of factors contribute to their relative popularity. Notably they have a relatively short generation time, are

genetically similar to humans, have a number of established models of human disease, are small in size, and have a variety of available transgenic strains. Particularly in the field of medical imaging, the commercial availability of small animal imaging systems has made pre-clinical imaging research even more attractive. These miniaturized versions of their clinical counterparts come at a reduced cost and are able to fit in small laboratory spaces.

1.6.2 Whole-Mouse Image Registration

Utilizing mice in medical imaging research has a number of interesting applications in both biological research and also in the development of novel imaging techniques. In both these cases, image registration of whole animal images can also be extremely useful. In terms of medical research, mice offer a unique opportunity to investigate highly controlled longitudinal effects of disease progression and response to therapeutic interventions. Non-invasive imaging can play an important role in this research as animals can be imaged at regular time intervals, serving as their own controls over time. However, for the results from each time to be compared the images should be accurately registered; compensating for postural and anatomical changes that have occurred between imaging sessions.

Another situation in which registration of mice may to prove to be extremely useful is in multi-modal imaging. While the motivation here is not necessarily specific to mice; registering images from different modalities will combine information from multiple sources, each of which exploiting a unique quality of the imaged anatomy. The implications of this were discussed previously in regard to MRI and histological

applications but the same concepts apply to combinations of other imaging modalities as well.

While these motivating factors could apply to imaging and registration of any isolated portion of anatomy, such as the abdomen, head, or an extremity which is similar to what is done clinically, whole animal approaches offer some unique advantages. In terms of image processing, development of robust whole animal techniques can circumvent the need to develop multiple tools specific to each anatomical application. Alternatively, as a tool for investigating biological processes, whole animal investigation may provide a more comprehensive view of diseases affecting multiple tissues simultaneously.

However, registration of whole animal images has unique challenges, most notably the presence of a number of articulated structures (joints). These anatomical features provide a relatively large range of unrestricted motion which must be accounted for in registration. One approach to addressing this has been to extract and align the mouse skeletons[27, 28] Presumably, because the skeleton provides the structural framework for the rest of the body and is composed of a finite number of rigid components, once it has been aligned this should compensate for postural differences between the two images and provide a good initialization for subsequent conventional approaches. This approach is particularly suited to CT images because they offer high contrast between bony structures and soft tissue, making extraction of the skeleton easier.

Approaches have also been implemented for the MRI images[29]. These however do not rely on skeletal identification. Rather, images are aligned in hierarchical fashion where the volumes are aligned in increasingly smaller sections, corresponding to different levels of anatomical detail. Similarly, a piece-wise registration approach has been used[30] to compensate for displacement of head and extremities between different modalities. Typically, clinical images are not or cannot depict the entire body in one continuous image. This likely contributes to the relatively limited number of papers focusing on whole animal registration as the approaches cannot be directly translated from human applications. However, the above mentioned approaches have proven to be successful and demonstrate a number of situations in which whole animal imaging is not only possible but valuable.

1.7 Thesis Objective

Both registration addressing whole mouse images, and multi-modality registration between MRI and histology have significant obstacles in achieving accurate alignment. While both have been addressed in different applications, attempts to align whole mouse histological sections with *in vivo* MRI have not been made. In this thesis I examine the feasibility of registering whole mouse histological sections with 3D MR volumes using an optical volume intermediate (figure 1.5). At present, a manual technique has been developed which can be used to accurately register histological sections with their corresponding 2D optical images[31]. For that reason, this thesis will focus solely on the registration of the MR and optical image volumes. Here, I implement and validate a fully automated registration algorithm to accurately co-register these two volumes as an initial step towards whole mouse MRI and histological registration.
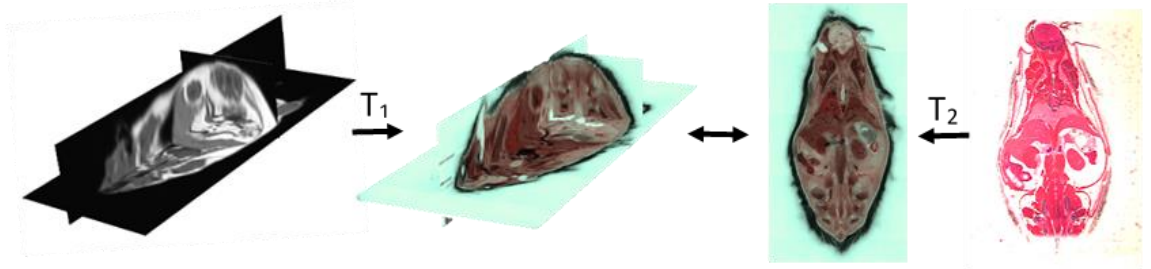
Figure 1.5: Overview of proposed co-registration approach for whole mouse histological and 3D MR images. Transformation T_1 maps the MR volume with the corresponding optical cryo-section volume. Histological sections are mapped to the corresponding 2D optical image, which is a single slice from the 3D optical volume, via a different transformation T_2.

1.8 Thesis Outline

Chapter 2 will provide a description of general image registration approaches, implementation and validation techniques.

Chapter 3 is a more detailed description of the implementation used here for the registration of whole mouse optical and MR image volumes as well as the results of experimental studies.

Chapter 4 provides a review of important findings as well as insight into future work related to this project.

1.9 References

1.   Mescher, A. and L.C.U. Junqueira, *Junqueira's basic histology : text & atlas*. 12th ed. 2010, New York: McGraw-Hill Medical. x, 467 p.

2.   Nafie, S., et al., *The role of transperineal template prostate biopsies in prostate cancer diagnosis in biopsy naive men with PSA less than 20 ng ml(-1.).* Prostate Cancer Prostatic Dis, 2014. **17**(2): p. 170-3.

3.   Rakha, E.A., et al., *Breast cancer prognostic classification in the molecular era: the role of histological grade.* Breast Cancer Research, 2010. **12**(4).

4.   Saleh, H.A. and A.H. Abu-Rashed, *Liver biopsy remains the gold standard for evaluation of chronic hepatitis and fibrosis.* Journal of Gastrointestinal and Liver Diseases, 2007. **16**(4): p. 425-426.

5.   Loeb, S., et al., *Complications After Prostate Biopsy: Data From SEER-Medicare.* Journal of Urology, 2011. **186**(5): p. 1830-1834.

6.   Thampanitchawong, P. and T. Piratvisuth, *Liver biopsy:complications and risk factors.* World J Gastroenterol, 1999. **5**(4): p. 301-304.

7.   Corcoran, N.M., et al., *Underestimation of Gleason score at prostate biopsy reflects sampling error in lower volume tumours.* BJU Int, 2012. **109**(5): p. 660-4.

8.   Regev, A., et al., *Sampling error and intraobserver variation in liver biopsy in patients with chronic HCV infection.* Am J Gastroenterol, 2002. **97**(10): p. 2614-8.

9.   King, C.R. and J.P. Long, *Prostate biopsy grading errors: a sampling problem?* Int J Cancer, 2000. **90**(6): p. 326-30.

10.   Webb, R.H., *Confocal optical microscopy.* Reports on Progress in Physics, 1996. **59**(3): p. 427-471.

11.   Castleman, K.R., *Concepts in imaging and microscopy: Color image processing for microscopy.* Biological Bulletin, 1998. **194**(2): p. 100-107.

12.   Heintzmann, R. and G. Ficz, *Breaking the resolution limit in light microscopy.* Digital Microscopy, 3rd Edition, 2007. **81**: p. 561-+.

13.   Schulz, R.B. and W. Semmler, *Fundamentals of optical imaging.* Handb Exp Pharmacol, 2008(185 Pt 1): p. 3-22.

14.   Lichtman, J.W. and J.A. Conchello, *Fluorescence microscopy.* Nat Methods, 2005. **2**(12): p. 910-9.

15.   Haacke, E.M., *Magnetic resonance imaging : physical principles and sequence design.* 1999, New York: Wiley. xxvii, 914 p.

16.   Costa, D.N., et al., *Body MRI using IDEAL.* American Journal of Roentgenology, 2008. **190**(4): p. 1076-1084.

17.   Maes, F., D. Vandermeulen, and P. Suetens, *Medical image registration using mutual information.* Proceedings of the Ieee, 2003. **91**(10): p. 1699-1722.

18.   Zhou, L., et al., *Liver Dynamic Contrast-Enhanced MRI for Staging Liver Fibrosis in a Piglet Model.* Journal of Magnetic Resonance Imaging, 2014. **39**(4): p. 872-878.

19.   Goubran, M., et al., *Image registration of ex-vivo MRI to sparsely sectioned histology of hippocampal and neocortical temporal lobe specimens.* Neuroimage, 2013. **83**: p. 770-781.

20.   Alic, L., et al., *Multi-modal image registration: matching MRI with histology.* Medical Imaging 2010: Biomedical Applications in Molecular, Structural, and Functional Imaging, 2010. **7626**.

21.   Jager, G.J., et al., *Local staging of prostate cancer with endorectal MR imaging: Correlation with histopathology.* American Journal of Roentgenology, 1996. **166**(4): p. 845-852.

22.   Gibson, E., et al., *Registration of prostate histology images to ex vivo MR images via strand-shaped fiducials.* Journal of Magnetic Resonance Imaging, 2012. **36**(6): p. 1402-1412.

23.   Coombs, B.D., et al., *Structure of plaque at carotid bifurcation - High-resolution MRI with histological correlation.* Stroke, 2001. **32**(11): p. 2516-2521.

24.   Choe, A.S., et al., *Accuracy of image registration between MRI and light microscopy in the ex vivo brain.* Magnetic Resonance Imaging, 2011. **29**(5): p. 683-692.

25.   Jacobs, M.A., et al., *Registration and warping of magnetic resonance images to histological sections.* Medical Physics, 1999. **26**(8): p. 1568-1578.

26.   Breen, M.S., R.S. Lazebnik, and D.L. Wilson, *Three-dimensional registration of magnetic resonance image data to histological sections with model-based evaluation.* Annals of Biomedical Engineering, 2005. **33**(8): p. 1100-1112.

27.   Baiker, M., et al., *Fully automated whole-body registration in mice using an articulated skeleton atlas.* 2007 4th Ieee International Symposium on Biomedical Imaging : Macro to Nano, Vols 1-3, 2007: p. 728-731.

28.   Li, X., et al., *Automatic nonrigid registration of whole body CT mice images.* Med Phys, 2008. **35**(4): p. 1507-20.

29.   Kovacevic, N., G. Hamarneh, and M. Henkelman, *Anatomically guided registration of whole body mouse MR images.* Medical Image Computing and Computer-Assisted Intervention - Miccai 2003, Pt 2, 2003. **2879**: p. 870-877.

30.   Dogdas, B., et al., *Digimouse: a 3D whole body mouse atlas from CT and cryosection data.* Physics in Medicine and Biology, 2007. **52**(3): p. 577-587.

31.   Eli Gibson, *e.a.*, *3D Co-Registration of MRI and Histology in a Mouse Model of Obesity and Non-Alcoholic Fatty Liver Disease.* Proceedings of the International Society of Magnetic Resonance in Medicine, 2013. **21**: p. 3729.

Chapter 2 :

Image Registration

2.1 Types of Registration

As previously mentioned, there are a wide variety of applications for image registration. Consequently, there are also a large number of registration methods that can be used, most of which are specifically tailored to a distinct problem. While there are a number of proposed methods, most can be classified into a few broad categories of approaches that have been developed. The choice of which to use will be dependent on the images being registered.

28

2.1.1 Feature Based

A common approach to registration are feature based methods. These techniques extract salient homologous features in the images to guide alignment. Features are typically points[1], lines or curvature that can be reliably and easily identified in both images[2, 3]. Once these corresponding features have been identified, the registration can proceed to find the optimal transformation to bring them together.

Ultimately, the success of this approach is dependent upon what features can be extracted from the images[4]. For a feature to be appropriate it should be easily and reliably identifiable in both images. This may be more challenging to address in multimodal problems as the appearance or saliency of features may drastically change in different modalities[5]. Moreover, there must be a number of identifiable features spread over the area of the image to achieve accurate alignment over the entire field of view. If these criteria cannot be addressed, using another approach may be more appropriate.

2.1.2 Intensity Based

Alternatively, if features cannot be easily extracted from the images an intensity based method may be employed. In these methods, the individual intensities of all overlapping pixels in a given alignment will be used to calculate some similarity metric. When images are optimally aligned, this metric should reach a global maxima, making this approach in essence an optimization problem.

These methods look at the individual pixel intensities as independent entities unrelated to other pixels and each weighted equally in the metric calculation. This approach makes the implementation of intensity based calculations relatively straightforward, but may overlook higher order relationships between pixels which may important to consider in an optimal registration[6].

Moreover, because this method looks exclusively at pixel intensities, anything that will affect these intensities will also have an effect on the registration. Some things to consider in this regard are image noise, changes to the sensor and differences in the illumination. While these factors can be addressed by altering portions of the implementation, it is important to acknowledge their potential effect.

2.1.3 Finite Element Method

A less commonly used approach is finite element method (FEM). As the name alludes to, FEM attempts to model the anatomy of interest by defining finite number of discrete units over its volume. Each of these units is assigned a set of physical properties that have been experimentally determined based on the tissues being imaged. Once the tissue of interest has been divided into discrete units and defined, the mechanical properties of the tissue under an applied force can be accurately modelled. Theoretically this approach works under the premise that if the volume is divided into small enough sections, and the location of each section can be determined, this will accurately approximate the behaviour of the tissue as a whole. The advantage of this approach is that it can closely model the

mechanical behaviour of the tissue and restrict the registrations to those that are physically plausible under the given conditions. In particular, this approach has been shown to be useful in modelling soft tissue deformation[7].

While having the potential to be extremely accurate, FEM registrations require a substantial amount of work to construct. Over the image of interest a number of physical parameters defining different tissues need to be determined and assigned. As a result, FEM has limited applications. Considering the current problem, determining, defining and delineating all the tissue types over the entire animal would be extremely tedious. Moreover, because FEM registrations model the behaviour of each finite unit, computational times can be extremely long.

2.2 Intensity Based Registration Framework

Although there is a large amount of variability even within the category of intensity based registrations, generally these can be broken down into a combination of a few basic components as seen in figure 2.1. The most obvious of these components are the two input images. Conventionally, one of these images is labelled the "fixed" image and remains stationary throughout the registration process. The other image is labelled "moving" and is transformed to spatially align with the fixed image. Other components include the transform, metric, interpolator and optimizer. Each component has a set function within

the registration algorithm, which will be described in more detail, but may be implemented differently to meet the demands of a given problem.
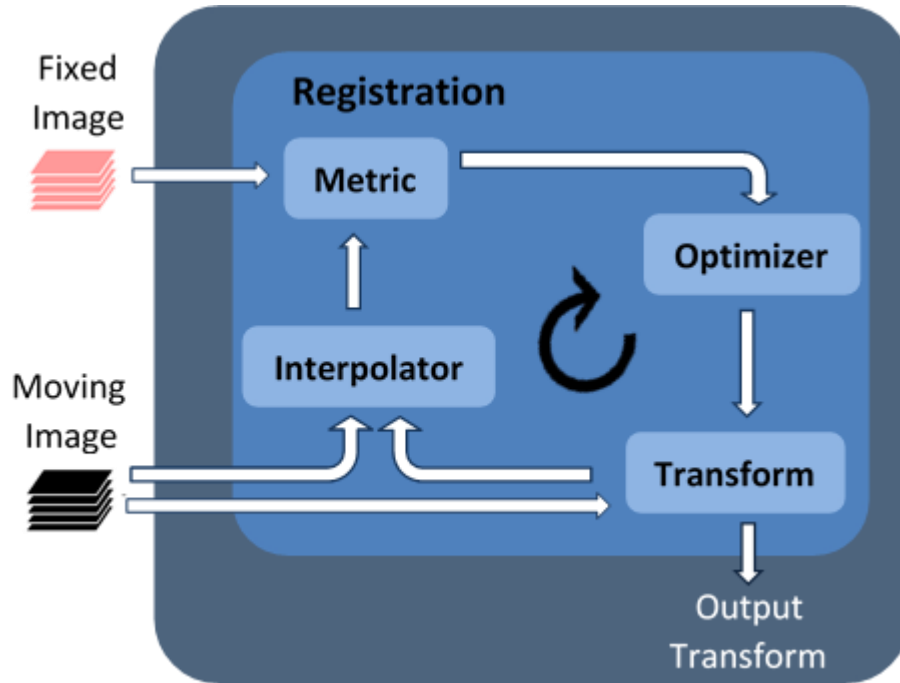
Figure 2.1: Block diagram of basic intensity-based registration components. During each iteration of the algorithm, a new transform is proposed by the optimizer and applied to the moving image resulting in a new alignment between the two input images. This alignment is then compared to other candidate alignments using the calculated metric value. This process is continued until the stopping criteria has been met at which point the transform determined to have the most favorable metric value is supplied as output.

2.3 Transforms

Transforms define how the moving image may be manipulated to align with the fixed image. Once registration is complete, this will spatially map all the points from one image

to the other. The purpose of the image registration process is to determine the numerical parameters of the transform that will optimally align the images. There are a few types of transformations, each of which is slightly different in terms of how much restriction is placed on the transformation.

2.3.1 Rigid

Rigid transformations refer to those in which each point in an image is transformed equally, maintaining the image's original pixel arraignment and spacing. As a result, transformations are limited to rotation and translation. These transformations are capable of accurately registering structures such as bone, which have a relatively fixed geometry[8]. Conversely, they are not capable of compensating for more localized deformations that occur in soft tissues.

2.3.2 Affine

Slightly less constrained than rigid transformations, affine transformations permit translation and rotation and also incorporate shear and scaling. These transformations do not necessarily maintain the original spacing of the image but do maintain parallel lines. Again these transformations are applied globally over the image and as a result cannot compensate for localized deformation.

2.3.3 Non-rigid

Non-rigid transformations encompass all geometric transformations which are not applied globally over the entire volume. The advantage of these transformations is their ability to compensate for more localized deformations; making them particularly important for soft tissue registration. They are also important for multi-modal problems were it is unlikely patient posture can be sufficiently restrained between imaging sessions.

There are a number of approaches to non-rigid registration. In particular, B-splines have been shown to be useful in medical image registration problems because they can model localized deformations[9]. Implementation of B-splines involves defining a coarse uniformly spaced grid over the image volume as demonstrated in figure 2.2. At intersections of the grid lines are "control points" which are used to define the displacement of the tissue. The location of these control points can then be manipulated until an optimal alignment is achieved. Between these points cubic splines will interpolate intensities to achieve a smooth displacement field. By enabling the transformations to have a spatially varying magnitude, localized deformations can be more appropriately represented.

It is common for multiple transformations to be combined in series to achieve a desirable registration[10]. Particularly, rigid or affine transformations will precede non-rigid registrations. In doing this the images can be coarsely aligned using a transformation that requires less processing time, giving a good initialization for more complex non-rigid transformations.
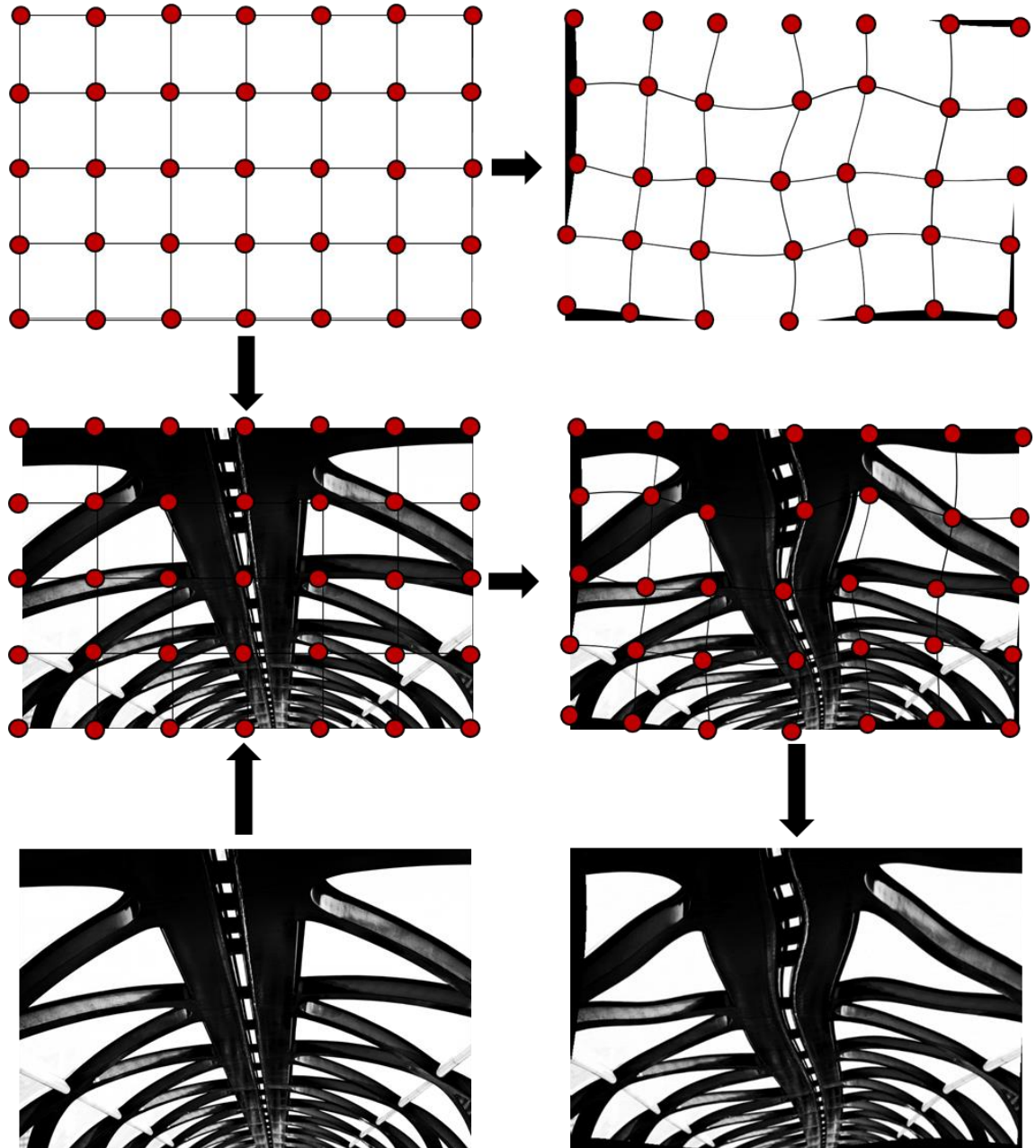
Figure 2.2: An example of image warping using B-splines. The top row shows the B-spline grid of control points (indicated by red dots). In the image on the right the control point have been displaced from their original locations (left) causing the underlying grid to warp. An overlay of the control point grid on an example image can be seen in the middle row before and after control point displacement respectively. Finally the bottom row shows the original image (left) and resulting B-spline warped image (right). *(Original Photograph Courtesy of Suzannelizabeth Photography).*

2.4 Metrics:

As stated previously, the purpose of an image similarity metric is to quantify how well a given transformation aligns two images; providing a way to compare the accuracy of candidate transformations. This serves as a cost function to be maximized or minimized (depending on the metric) to achieve accurate alignment. For intensity based registrations, these metrics are generally calculated from all overlapping pixels in aligned images. There are a number of possible metrics to use, each of which is suited to a different type of registration problem.

2.4.1 Mean Squared Error

The simplest of the similarity metrics is mean squared error (MSE). This is computed by calculating the mean of the squared difference between intensity values of overlapping pixels:

$$MSE(A, B) = \frac{1}{N} \sum_{i=1}^{N} (A_i - B_i)^2$$

Where A_i is the i-th pixel of image A, B_i is the i-th pixel of image B, and N is the number of overlapping pixels from A and B. This metric will equal zero when images are perfectly aligned. While relatively computationally inexpensive, leading to lower registration time, MSE is not particularly robust and as a result is only suitable for a narrow range of potential applications. MSE is only appropriate in registration problems where the two

images being registered have the same contrast. Inherently, this makes MSE inappropriate for multi-modality registration problems and as such would not be used for the MRI-optical registration being undertaken here.

2.4.2 Normalized Cross-Correlation

A slightly more robust metric is normalized cross-correlation (NCC). This metric is calculated as:

$$NCC(A,B) = \frac{1}{N}\sum_i \frac{(a_i - \bar{a})(b_i - \bar{b})}{\sigma_a \sigma_b}$$

Here a_i and b_i are overlapping pixels, σ_a and σ_b are the standard deviations in image intensity, and $\bar{a}$ and $\bar{b}$ are the intensity means from images A and B respectively. By incorporating the mean and standard deviations of the two image intensities this metric is capable of compensating for scaling factors in intensity values between images. As a result NCC is more appropriate for unimodal registration problems, as it can accommodate some changes between signal intensities. However, like MSE, NCC relies on a relationship between the intensity values of the two images and as such is not appropriate for multi-modal problems.

2.4.3 Mutual Information

Unlike either MSE or NCC, mutual information (MI) does not assume any relationship between pixel intensities of the two images. This quality makes mutual information particularly suited to multi-modal image registration problems where direct comparison of grey scale values is inappropriate. Particularly, it has been shown as an effective metric for registration problems involving histological and MR images[11, 12].

MI is an information theory measure of statistical dependence between the two images. It will measure how well one image is able to explain the other. To measure the information contained in a single image, the Shannon entropy[13] can be used:

$$H = -\sum_i p_i \log p_i$$

Here p_i is the probability of event i, which in the case of images refers to how often a given intensity value occurs. This can be calculated from a histogram of image intensities, where the probability will be the number of times an intensity value occurs in the image divided by the total number of pixels. Entropy will reach a maxima when intensity values are equally distributed throughout all grey scale values. In the case of overlapping images the joint entropy can be calculated:

$$H(A, B) = -\sum_{i,j} p_{i,j} \log p_{i,j}$$

Here $p_{i,j}$ is the probability of event i,j occurring, which is the combination of two overlapping pixel intensities. To quantify this, a feature space[14] can be constructed in which intensity values from overlapping regions of the images are placed in to a 2D plot. This feature space is a joint intensity histogram, which will effectively count the number
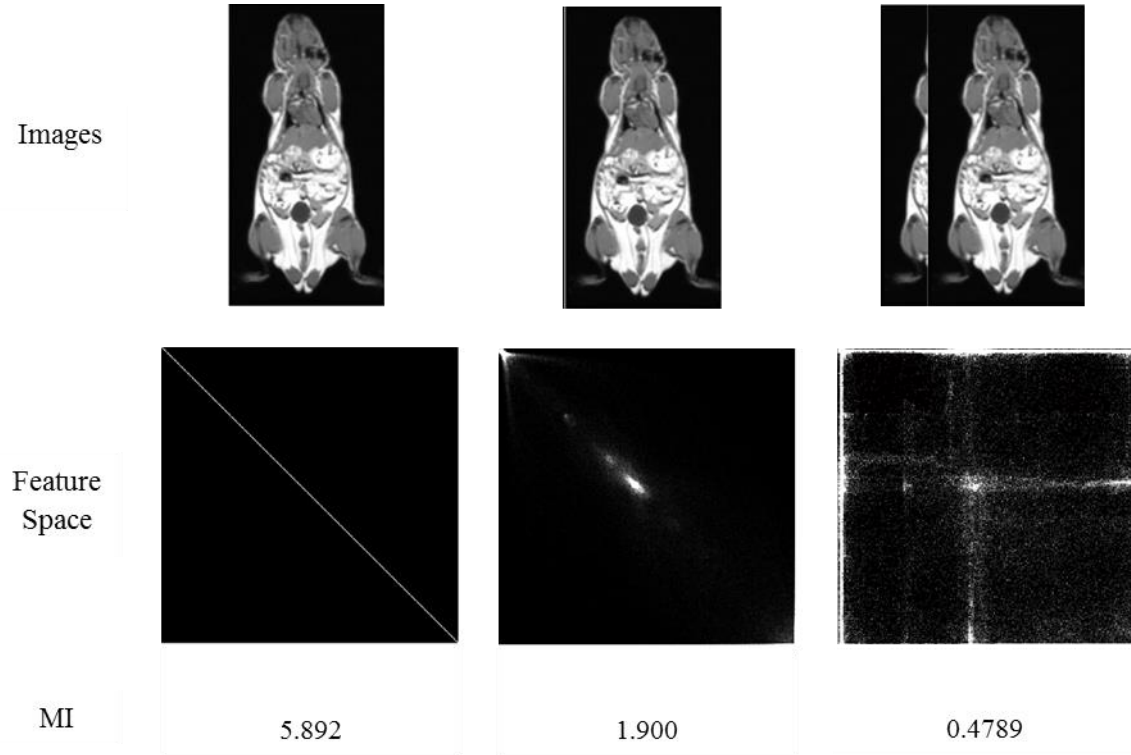
Figure 2.3: A demonstration of the relationship between image alignment, feature space and the mutual information metric. The top row shows the alignment of a single coronal T1w MR image with itself and the associated joint intensity histogram feature space and metric value below. The left column corresponds to perfect alignment of the two images, resulting in a clustered feature space and high metric value. In the second column images have been translated by five pixels resulting in a more dispersed feature space and lower metric value. Finally in the right column images have been translated by 100 pixels leading to a large degree of scattering in the feature space and low MI value demonstrating the relationship between the image alignment and metric value.

of occurrences of each combination of intensity values in aligned pixels. Again, this will be maximized if there is a large, even distribution of intensity combinations. Compared with joint entropy, mutual information constrains the marginal entropies of both images to discourage registrations where images are completely misaligned.

$$MI(A, B) = H(A) + H(B) - H(A, B)$$

Here H(A) and H(B) are the marginal entropies of images A and B respectively and H(A,B) is the joint entropy of the two images. Like the marginal entropies, joint entropy will be maximized when there is an even distribution of intensity combinations spread throughout the feature space. However, in the MI equation the joint entropy is inversely related to MI. Therefore, to maximize MI joint entropy should be minimized, which will occur when there are few but frequent combinations of intensity values which is demonstrated in figure 2.3. When the images are optimally aligned in the first column, a small number if histogram bins in the feature space have high values and MI is high. Conversely, as the images are moved away from this optima, the clusters of high bin values will decrease and spread out over other bins. This is reflected then in the MI calculations as the joint entropy increases with increased dispersion in the feature space and MI decreases.

Conceptually, the metric reaches an extreme when regions of similar intensities within one image align with another relatively homologous region in the other image. Again, this does not rely on the actual intensities of the regions to be compared, but instead quantifies how often combinations of pixel intensities occur. For example, medical images capture a view of tissues and organs; each of which is composed of similar cells and structures and as a result should have a relatively consistent intensity across its volume. While the specific intensity is dependent on the modality, we can assume that each tissue will have some sort of characteristic range of values within a given image. Figure 2.4 demonstrates this relationship between the tissue intensities in the feature space. When images are aligned (figure 2.4 left) the same anatomy in the two images will align resulting in a clustering of frequent intensity value combinations. Conversely, when images are unregistered (figure 2.4 right) the intensity combinations are less frequent and more spread out in the feature space. MI is able to quantify this clustering of the feature space, providing a way to quantify image alignment without relying on a direct relationship between intensity values of aligned pixels.
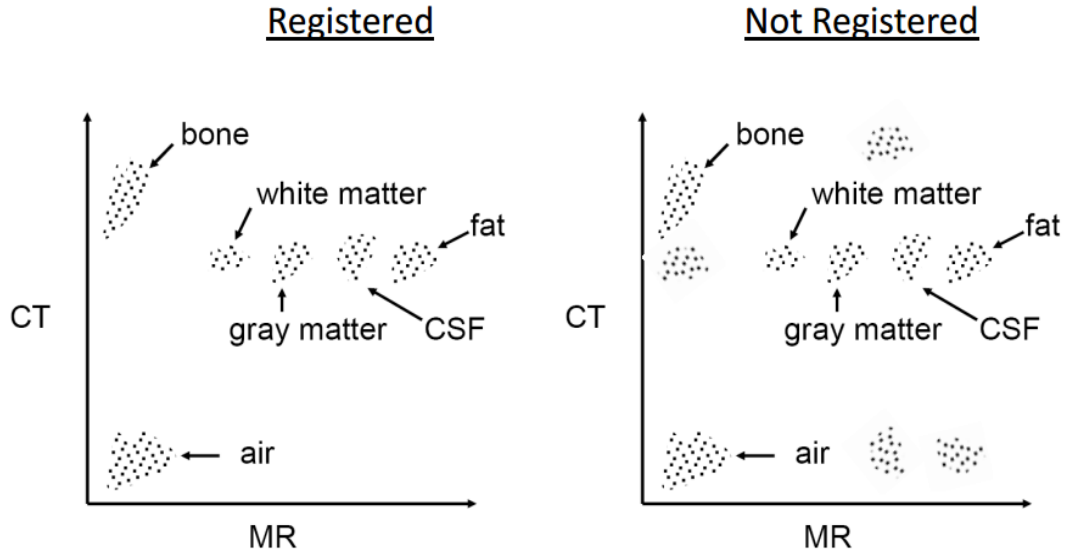
Figure 2.4: A depiction of the relationship between intensity values and image alignment in multi-modality registration. Each tissue type has a characteristic range of intensity values in each modality. When images are registered (left) intensities from the same tissue type align resulting in few small clusters if intensity combinations. Alternatively, when the images are unregistered (right) the tissues do not align and the intensity clusters spread out. *(Source: W. Wells, MICCAI 2009)*

2.5 Interpolators

The metric value for a given alignment is calculated from overlapping intensity values in the two input images. These intensity values are determined by mapping the grid-points from the fixed image space to the corresponding locations in the moving image as described by the current transform. In general, this mapping will not be to a grid position

in the moving image and as such will not have an assigned intensity value. To mitigate this, a strategy to determine non-grid position intensities needs to be specified, which is the purpose of the interpolator.

Nearest neighbor is the easiest interpolation approach in which the intensity value from the closest grid point is used. While computationally inexpensive, this approach imposes a discretized view of image intensity where values are constant and jump mid-way between grid points, which is not necessarily reflective of the underlying tissue.

Alternatively, linear interpolation approaches determine intensities assuming linear variation between grid points. This method of interpolation is still relatively computationally inexpensive and allows for spatial continuity in intensities between grid points. However, this will result in discontinuity at grid points.

It is also possible to use higher order interpolators including cubic B-spline and sinc functions. These methods will result in spatially continuous intensities across the image space. However, this comes at the cost of increased computational time. Because the metric will be calculated on each iteration, requiring interpolation to be used in the process, the interpolation strategy can have a large effect on the computational time and should be considered. Despite being potentially more accurate[15] a computationally less demanding approach may be chosen, given the considerable increase in time required. Moreover, because mutual information is calculated from binned intensity values in the

joint intensity histogram, more accurate interpolation may not necessarily translate to a more accurate metric calculation due to rounding during binning[16].

2.6 Optimizers

Theoretically, each metric has a finite value that defines the perfect registration. However, due to the inclusion of noise and other imperfections this value is generally unattainable in practice, even with the optimal transformation. The goal of intensity based registrations is then to achieve optimal alignment of the two images by finding the global extreme of a given similarity metric. Optimizers define the strategy for finding this extreme within the scope of allowable transformations or the parameter space. Figure 2.5 shows an example parameter space for a transformation including only translations in two dimensions.

The general approach in a registration algorithm is to use an iterative method depicted in figure 2.1, where a new transformation is proposed based on the optimizers strategy and tested against the current transformation based on the calculated metric. This process is continued until some sort of convergence criteria is achieved indicating an acceptable transformation has been reached.

One approach is an exhaustive search strategy, where every possible transformation within the parameter space is tested. While this strategy is easy to implement and guarantees finding the optimal solution, the computational time can be very long,

especially for non-rigid registration problems which generally have a large parameter space.

Alternatively, more sophisticated methods can be used to traverse the parameter space in search of the optimal transformation. One such method is the gradient descent approach. This method takes a step in the direction of the largest negative gradient to move towards the minimum[17]. This process is continued until the gradient decreases to zero at which time it is assumed the minimum has been converged upon. The step size on each iteration is a function of the current gradient magnitude. When the gradient is large so is the step size, and as the gradient converges upon zero, the step size decreases.

A modification to this approach is the regular step gradient descent optimizer. Like the gradient descent optimizer, this approach will move in the direction of the largest negative gradient. However, the step size in this approach is not dependent on the magnitude of the gradient at any time. Rather, the step size is decreased by constant factor at each iteration; the gradient only determines the direction of the step in this approach. The user in this case specifies a starting and stopping step size, and in the process specifies the

convergence criteria. This approach is less reliant on the shape of the cost function and may improve efficiency in some cases.
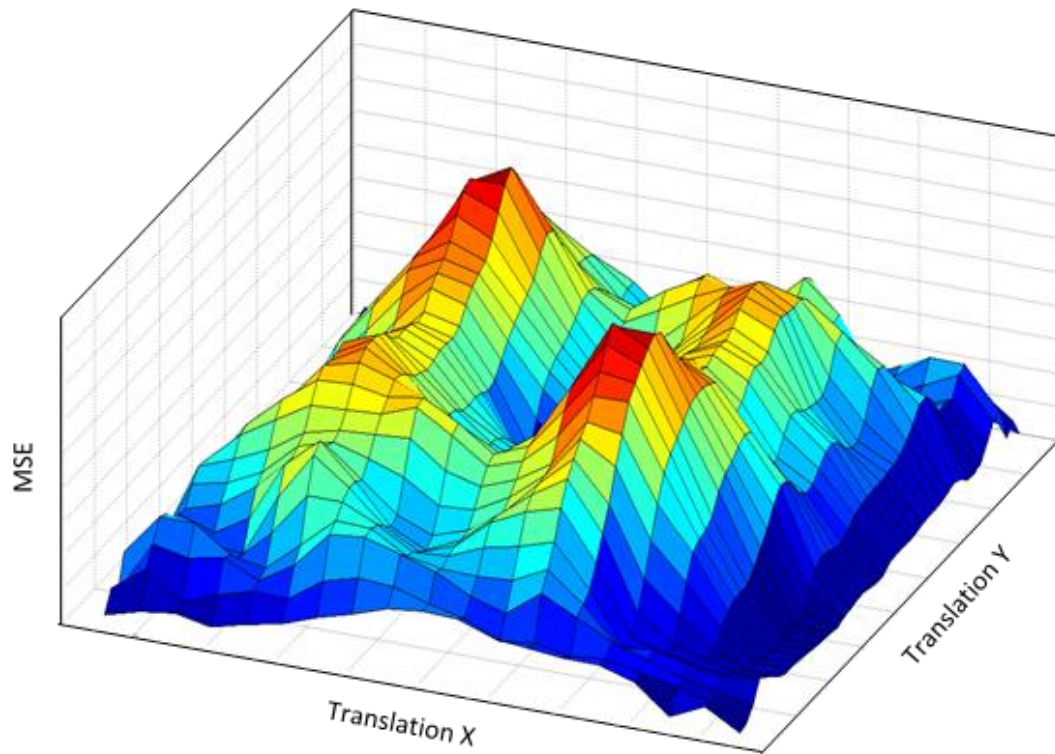
Figure 2.5: Surface plot of MSE values calculated from two copies of a single image aligned by translations in the X and Y axis. In the center of the plot, the large valley corresponds to the optimal alignment of the images and the metric minimum.

Unfortunately, because the optimal value of the similarity metric is unknown none of these strategies can guarantee convergence onto the optimal transformation, or within acceptable proximity. One of the major problems with these techniques is that because the cost functions are hardly ever smooth, optimizers may stop at local extremes assuming

they have converged upon the optima. Similarly, if the registration is initialized poorly the optimizer may move away from the optimal alignment. This would occur if the registration were to be initialized around the perimeter of the parameter space depicted in figure 2.5; as the optimizer would descend towards the edges of the parameter space reaching incorrect minima. In both cases, this will return an incorrect set of parameters as the optimal transformation. Despite this risk, optimization strategies are almost always employed as a result of the extremely time consuming process of exhaustive searches.

2.7 Image Preprocessing

An optional component of the registration framework is the incorporation of any number of image preprocessing operations. This encompasses a wide variety of operations that can be performed on images prior to registration to improve accuracy. These include things such as smoothing filters, edge detection and deblurring.

While these components are all optional, there is one preprocessing step that is required to implement an intensity based registration optimizing MI as outlined previously. In the explanation of the metric calculations, they are formulated to compare two images in which the pixel intensities are expressed as single values, such as the case in grey scale images. However, the optical images have intensity values expressed as a vector with values for red, green and blue. While this does enable representation of color images, it also means that optical images need to be converted to grey scale prior to attempting a mutual information based registration.

There are some different approaches to doing this. One is to use only one of the color channels (e.g. red) in the registration. While being easy to implement, this approach only considers a portion of the available contrast collected from the three channels. Alternatively, a luminance filter can be incorporated; converting images to greyscale by computing a linear combination of red, green and blue channels on a pixel-by-pixel basis. This approach incorporates information from all three channels without having a substantial effect on computational time.

2.8 Validation Methods

The goal of image registration is to accurately align two images. While visual inspection of the post registration anatomical agreement can assess the registration performance to some degree, it relies on qualitative assessment of the images. To quantify the registration accuracy, a number of metrics can be calculated, resulting in a meaningful value that can be used to compare and validate registration techniques.

2.8.1 Dice Similarity Coefficient

One common approach to registration validation is to calculate a dice similarity coefficient (DSC), which effectively quantifies the percent overlap between homologous anatomies. To do this, tissues of interest such as an organ like the kidneys or even a sub region like the hippocampus of the brain are segmented in both images being registered.

In the post registration images, the percent overlap of the two segmentations is quantified. DSC values range from 0 to 1, 0 being a very poor registration achieving no overlap and 1 achieving full overlap between homologous anatomies.

2.8.2 Target Registration Error

Another approach to quantifying registration performance is to calculate a target registration error (TRE). To do this, a number of anatomically homologous points are chosen in both the fixed and moving images prior to registration; these will serve as landmark pairs. The locations of the post registration landmarks are then determined and the distance between post-registration landmark pairs quantified.

Selection of the anatomical points should ensure that the landmarks are unique points that can be positively identified in both images. Compared to 2D images, the landmark selection can be greatly complicated in 3D as the landmarks must be points in 3D space, not simply intersections of structures with the 2D imaging plane. In the case of whole animal imaging, structures such as blood vessel bifurcations and centroids of small circular structures may serve as landmarks. Distribution of the landmarks should also be considered when selecting anatomy for TRE calculations. Densely grouping landmarks together may inaccurately represent the overall performance of the registration, as there may be a spatial variation in registration performance.

Compared with the DSC method of quantifying registration performance, TRE values can provide a more accurate depiction of the registration performance. Unlike DSC, TRE values examine very specific points of anatomy where DSC looks at larger regions. In this way, a DSC may be very high, indicating a high degree of overlap and suggesting a good registration, but the anatomy may actually have a completely different orientation where substructures are misaligned. This however can be captured by TRE as homologous points that are largely misaligned will increase the calculated value; indicating poor registration performance. Moreover, TRE values provide a more meaningful metric then DSC. The distance measure from TRE values provides insight into exactly how far structures are displaced, defining a margin of error for a given application. For these reasons, TRE was chosen as the metric for quantifying registration performance for this application.

2.8.3 Fiducial Localization Error

TRE values calculated in the manner described incorporate both the registration error as well as the error associated with landmark selection. Because landmarks are selected manually, their localization is subject to the operator's discretion. To determine the extent to which the operator's localization affects the TRE value, a fiducial localization error (FLE) should be quantified. To do this, landmarks should be reselected in multiple sessions and the variability between selections quantified. This will give an indication to what extent the TRE reflects variability in the selection of landmarks.

2.9 Conclusion

While many approaches have been discussed here, this is in no way an exhaustive overview of any of the topics covered. Many new methods and modifications to existing strategies continue to be developed to not only improve registration performance but also decrease computational time. Generally, there is not necessarily a correct way to implement registration for a specific problem; often many approaches will be capable of providing an acceptable alignment. Rather, the specific problem should direct the choices for any component taking into consideration the required accuracy and computational time. In the next chapter I propose and validate a specific implementation for an intensity based registration to align 3D whole mouse optical and MRI volumes.

.

2.10 References

1. Vujovic, N. and D. Brzakovic, *Establishing the correspondence between control points in pairs of mammographic images.* Ieee Transactions on Image Processing, 1997. 6(10): p. 1388-1399.

2. Maintz, J.B. and M.A. Viergever, *A survey of medical image registration.* Med Image Anal, 1998. 2(1): p. 1-36.

3. Zitova, B. and J. Flusser, *Image registration methods: a survey.* Image and Vision Computing, 2003. 21(11): p. 977-1000.

4. Li, H., B.S. Manjunath, and S.K. Mitra, *A Contour-Based Approach to Multisensor Image Registration.* Ieee Transactions on Image Processing, 1995. 4(3): p. 320-334.

5. Rignot, E.J.M., et al., *Automated Multisensor Registration - Requirements and Techniques.* Photogrammetric Engineering and Remote Sensing, 1991. 57(8): p. 1029-1038.

6. Rueckert, D., et al., *Non-rigid registration using higher-order mutual information.* Medical Imaging 2000: Image Processing, Pts 1 and 2, 2000. 3979: p. 438-447.

7. Schnabel, J.A., et al., *Validation of nonrigid image registration using finite-element methods: Application to breast MR images.* Ieee Transactions on Medical Imaging, 2003. 22(2): p. 238-247.

8. Rajapakse, C.S., et al., *Efficient 3D rigid-body registration of micro-MR and micro-CT trabecular bone images - art. no. 69142Z.* Medical Imaging 2008: Image Processing, Pts 1-3, 2008. 6914: p. Z9142-Z9142.

9.   Rueckert, D., et al., *Nonrigid registration using free-form deformations: Application to breast MR images.* Ieee Transactions on Medical Imaging, 1999. 18(8): p. 712-721.

10.   Lester, H. and S.R. Arridge, *A survey of hierarchical non-linear medical image registration.* Pattern Recognition, 1999. 32(1): p. 129-149.

11.   Meyer, C.R., et al., *A methodology for registration of a histological slide and in vivo MRI volume based on optimizing mutual information.* Mol Imaging, 2006. 5(1): p. 16-23.

12.   Dauguet, J., et al., *Three-dimensional reconstruction of stained histological slices and 3D non-linear registration with in-vivo MRI for whole baboon brain.* J Neurosci Methods, 2007. 164(1): p. 191-204.

13.   Shannon, C.E., *A Mathematical Theory of Communication.* Bell System Technical Journal, 1948. 27(4): p. 623-656.

14.   Hill, D.L.G., C. Studholme, and D.J. Hawkes, *Voxel Similarity Measures for Automated Image Registration.* Visualization in Biomedical Computer 1994, 1994. 2359: p. 205-216.

15.   Thevenaz, P. and M. Unser, *Optimization of mutual information for multiresolution image registration.* IEEE Trans Image Process, 2000. 9(12): p. 2083-99.

16.   Tsao, J., *Interpolation artifacts in multimodality image registration based on maximization of mutual information.* IEEE Trans Med Imaging, 2003. 22(7): p. 854-64.

17.   Nocedal, J. and S.J. Wright, *Numerical optimization*. Springer series in operations research. 1999, New York: Springer. 636 p.

Chapter 3 :

Intensity Based Non-rigid Registration of 3D Whole Mouse Optical and MR Image Volumes

3.1 Introduction

Pathological evaluation of histology remains a gold standard for disease diagnosis and an important tool for research into the molecular underpinnings of disease. However, the need for animal sacrifice in tissue processing for histological preparation substantially limits longitudinal research studies investigating disease progression and the efficacy of

drug therapies. Novel MR imaging techniques may be able to address this short coming, enabling structural and molecular changes associated with disease to be elucidated non-invasively; allowing the animals to serve as their own controls. However, before these techniques can be used in place of histology, they must be validated, ideally via accurate co-registration with histological sections[1]. Moreover, co-registration of histology with *in vivo* MRI may prove to be extremely valuable in the development of MR based diagnostic tools, acting as a ground truth to analyze changes to MR contrast in different disease states[2-4].

However, registration of histology with *in vivo* MRI is challenging as a result of uncontrolled deformations introduced in 3D during histological tissue preparation and 2D as a result of the tissue sectioning procedure; both of which must be addressed to achieve accurate alignment. Often, an intermediate image volume is introduced to bridge the gap between histology and *in vivo* images which differ in resolution, contrast, and slice orientation. In many cases, an *ex vivo* MRI is acquired once the tissue of interest is fixed[5, 6] in an attempt to capture 3D distortions which have occurred as a result of histological processing; while maintaining consistent contrast and resolution. Alternatively, an optical image volume captured during cryo-sectioning[7-9] can be used as an intermediate. In this case, registration of the 3D optical and *in vivo* images will address 3D distortions incurred during tissue fixation, while 2D registration of histological images with the corresponding optical image will address deformation resulting from slicing.

In addition, cryo-sectioning techniques capable of whole animal processing may further simplify registration. Conventional histological processing techniques require the tissue of interest be isolated and processed independently from the rest of the body, introducing a number of uncontrolled 3D deformations in the process. While these deformations are unavoidable, they may be substantially reduced by leaving the animal intact, allowing tissues to be held in place by surrounding structures and also retaining anatomical context which may also be useful during registration. This approach may be particularly useful for tissues such as adipose and liver can become almost unrecognizably deformed when isolated from the body due to the tissue's low degree of stiffness[10, 11] and the lack of external constraints.

Furthermore, whole animal processing may prove advantageous in understanding the systemic effects of a number of diseases. Research into conditions such as cancer[12, 13] and obesity[14-16] continue to identify the importance of a complex whole body cellular and molecular interplay, which may be lost in a single tissue approach to investigation.

Of the two transformations required to co-register histology and MR images with the intermediate optical volume, we predict that the 3D MR-optical registration is the more difficult of the two. This registration must address drastic changes in contrast, and resolution as well as the inherent difficulty associated with an additional image dimension. Here we attempt to address this problem and investigate the feasibility of an image-based non-rigid registration method for whole animal 3D optical and MR image registration.

The effect of different MR contrasts on registration performance will be considered as well as a protocol for imaging. Combining this method with existing tools to manually register 2D histological slides with corresponding optical images[17] will provide a tool for accurate co-registration of histology and *in vivo* whole mouse MR images.

3.2 Materials

3.2.1 Animals

Imaging was performed on a total of nine mice, four of which were obese and the remaining five lean. Lean animals were fed a standard diet while obese animals were fed a western diet consisting of 42% calories from fat. Mice were either male strain C57Bl/6, or 129/SvJ. All experiments were conducted under a protocol approved by the institution's Animal Use Subcommittee.

3.2.2 MRI

MR imaging was performed at 3T using a Discovery MR750 (GE Healthcare, Waukesha, WI). Animals were imaged in a custom built mouse bird cage coil. Three image contrasts were collected: T1-weighted (T1w) 3D spoiled gradient echo (resolution: 0.6 x 0.6 x 0.7, TR: 6.2 ms, TE: 2.7 ms, pixel bandwidth: 244.141, Averages: 16, field of view (FOV): 100 x 55 x 32mm, slice thickness: 0.7mm, slice spacing: 0.7mm, matrix: 158 x 158, slices: 46, flip angle: 15 °) ; T2-weighted (T2w) fast spin echo (resolution: 0.8 x 0.8 x 0.7, TR: 2900ms, TE: 200 ms, pixel bandwidth: 244.141, averages: 10, FOV: 100 x 60 x 29mm,

slice thickness: 0.7mm, slice spacing: 0.7mm, slices: 42, flip angle: 90°); proton density weighted water-fat separated imaging acquired with an investigational version of IDEAL (resolution: 0.9 x 0.7 x 0.7, TR: 14.0ms, TE: 2.2ms, Pixel Bandwidth: 868.047, Averages: 13, FOV: 120 x 54 x 34mm, Slice thickness: 0.7mm, Slice Spacing: 0.7mm, Matrix: 140 x 176, Slices: 44, Flip angle: 3°).

3.2.3 Optical Imaging

Cryo-sectioning and optical imaging was performed on frozen tissue volumes using a Cryo-Viz™ cryo-imaging system (BioInvision, Cleveland Ohio, USA). Immediately following MR imaging, mice were prepared for cryo-sectioning using the manufacturer recommended protocol for tissue preparation and cryo-sectioning[18]. Sectioning was performed along the coronal plane of the mice with a 200μm slice thickness. High resolution optical images were acquired of the exposed face of the remaining tissue block with 17.5 μm in plane isotropic resolution resulting in a matrix size of approximately 3300 x 7100 x 180 (sagittal x axial x coronal).

3.3 Methods

3.3.1 Imaging Protocols

For two animals (one obese, one lean), MR imaging was performed while the animals were alive and anesthetized using isoflourane. Only IDEAL contrast images were collected for these animals. Immediately following MR imaging, these animals were euthanized and subsequently processed for cryo-sectioning as previously described.
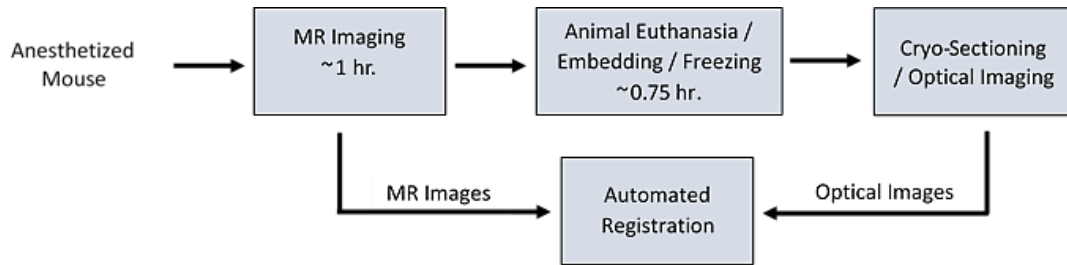
Figure 3.1: An overview of image acquisition and processing for animals in which MR imaging was performed prior to euthanasia. The approximate time required is also indicated.

In the remaining animals, all imaging was performed post-mortem as outlined in figure 3.2. All three MR contrasts were collected for these animals. Processing for cryo-sectioning was performed in the same way as animals imaged while still alive.
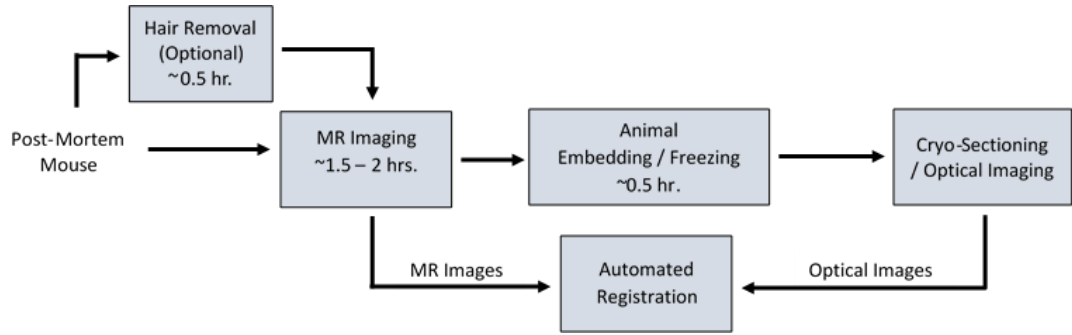
Figure 3.2: An overview of image acquisition and processing for animals imaged post-mortem with the approximate time required indicated

3.3.2 Registration

Prior to registration, animal hair was separated from tissue in optical images through segmentation either automatically, using software included in the Cryo-Viz^{TM} image processing software, or manually using 3D Slicer software (http://www.slicer.org/). Alternatively, a chemical hair removal procedure was performed following euthanasia and before MR imaging requiring approximately 30 minutes.

Optical images were down-sampled to an in-plane resolution of 0.21mm and a slice thickness of 0.8mm prior to registration. Volumes were initialized so animals in the two image volumes were oriented the same way in physical space.

In the registration algorithm, MR image volumes are aligned to the optical volume using a combination of rigid and non-rigid transformations. Registrations using IDEAL contrast were performed with the water-separated images. All portions of the registration, as

depicted in figure 3.3, were coded in C++ using implementations of the Insight Segmentation and Registration Toolkit (ITK; National Library of Medicine, Bethesda, MD). Optical images are initially converted to grey scale using a luminance filter and geometric centers of the image volumes aligned. Both rigid and non-rigid portions of the registration are performed using Mattes Mutual Information (MMI)[19] similarity metric. In this particular implementation of mutual information, the metric value will theoretically be minimized when the images are optimally aligned. The number of bins used for the MMI calculations was set to 50 and all voxels were sampled in the calculations. Linear interpolation was chosen for this implementation. Optimization was performed using a regular step descent gradient optimizer. For the rigid registration the minimum step size was set to 0.05.

The non-rigid portion of the registration was comprised of two consecutive B-splines of increasing grid size. The first B-spline had a control point grid with dimensions of 3x5x2 (sagittal x axial x coronal) and the second had 7x10x5. Parameters for this portion of the registration were consistent with the rigid portion except the minimum step size for the optimizer was set to 0.001 and 0.0001 for the first and second B-spline respectively.
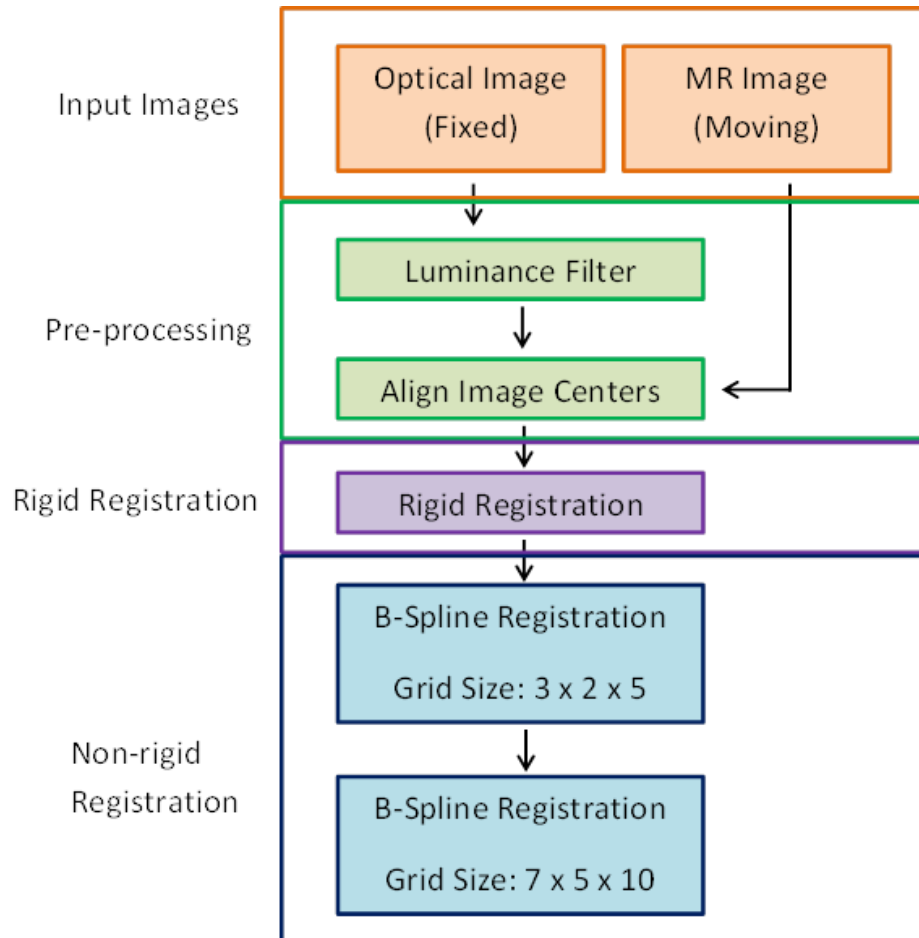
Figure 3.3: Flow chart of the intensity based image registration algorithm implemented in C++ showing the three main components pre-processing, rigid and non-rigid registration. Input optical images indicated here would have already been down sampled and segmented.

3.3.3 Validation

Registration accuracy was assessed by calculating a target registration error (TRE). TRE values were calculated as the post registration 3D Euclidean distance between anatomically homologous landmark pairs in corresponding optical and MR image volumes. Landmarks were manually chosen to be anatomically identical points identifiable by a human observer in both image modalities, which could be localized to a point in all three planes. Structures used as landmarks include, but are not limited to, centroids of small spherical structures such as eye balls, as well as vascular bifurcations and entrance points into tissues. In each of the MR-histology image pairs registered, 15-
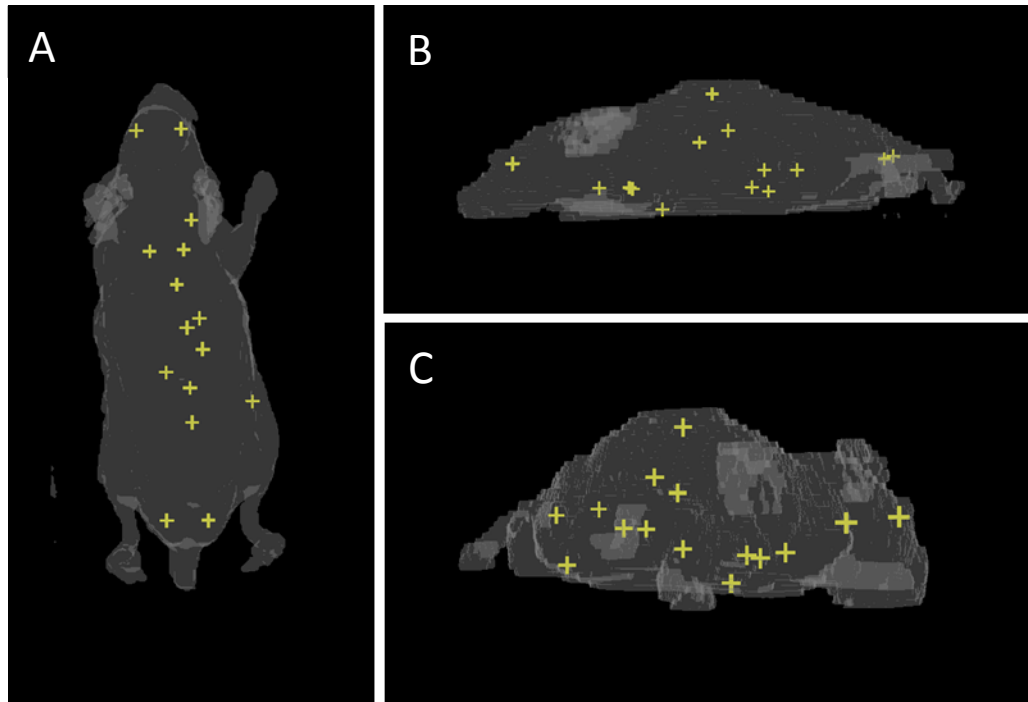
Figure 3.4: Distribution of landmarks used in TRE calculations for a single mouse in the (A) coronal, (B) sagittal and (C) oblique planes from a pre-registration optical image volume. The animal volume is shown in gray with locations of anatomical landmarks indicated by yellow crosses.

18 landmark pairs were identified for TRE calculations; yielding a total of 314 landmarks over 20 pairs of registered images. An example of the landmark distribution in a single animal can be seen in figure 3.4. For clarity, these points were not used in any way to register the images, they were only used for post-registration analysis.

TRE measurements incorporate error associated with the operator's ability to accurately select the landmark location. To quantify the inherent variability in landmark selection, the fiducial localization error (FLE) was calculated as an unbiased estimator of the standard deviation of repeated localizations of the same landmark[20]. For each image type (optical, T1w, T2w, IDEAL) all landmarks from three different randomly selected animals were reselected in six separate sessions, at least one day apart:

$$FLE = \sqrt{\frac{1}{J} \sum_{j=1}^{J} \frac{1}{K-1} \sum_{k=1}^{K} \left\| p_{j,k} - \frac{1}{K} \sum_{k=1}^{K} p_{j,k} \right\|^2}$$

Where $p_{j,k}$ is the kth localization of the j-th fiducial, J is the number of landmarks in a given image, and K is the number of repeated localizations of each landmark.

3.3.4 Statistical Analysis

Mean TRE and MMI values before and after the non-rigid portion of the algorithm were compared using paired two-tail t-tests. To compare the mean TRE values of the different MRI contrasts a repeated-measures analysis of variance (ANOVA) was performed. Post-hoc two-tailed t-tests were then done to determine the relative accuracy of registration using different MR contrasts. All statistical analysis was performed in Excel 2013 (Microsoft Excel. Redmond, Washington; Microsoft 2013).
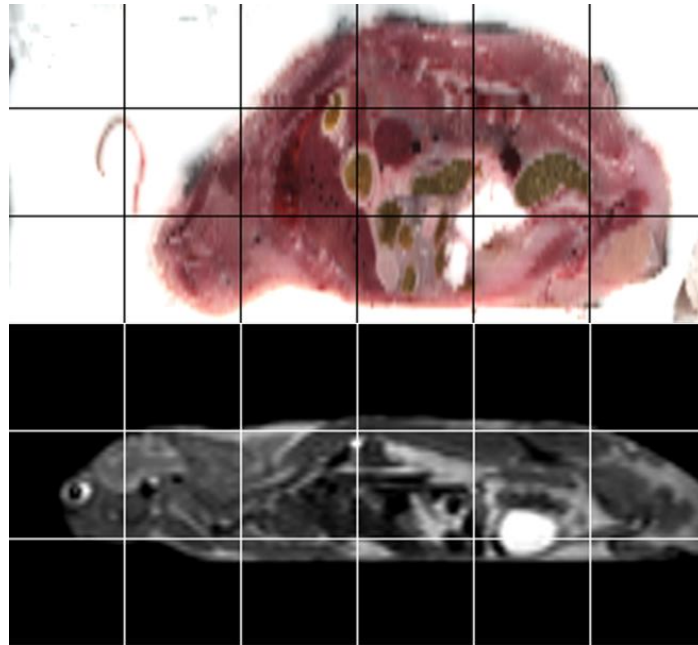
Figure 3.5: Sagittal view of corresponding optical (top) and T2w MR (bottom) images prior to image registration demonstrating the large degree of anatomical misalignment.

3.4 Results

Using the proposed method, registration of optical and MR image volumes was completed on average in under 7 minutes; in the longest case taking just under 15 minutes. In two cases automated segmentation of the optical tissue volumes failed and hair had not been removed prior to imaging. In these cases, manual segmentation was required to isolate hair from the underlying tissue, taking approximately one hour to complete. In later animals hair was removed prior to imaging to eliminate the need for tissue segmentation.
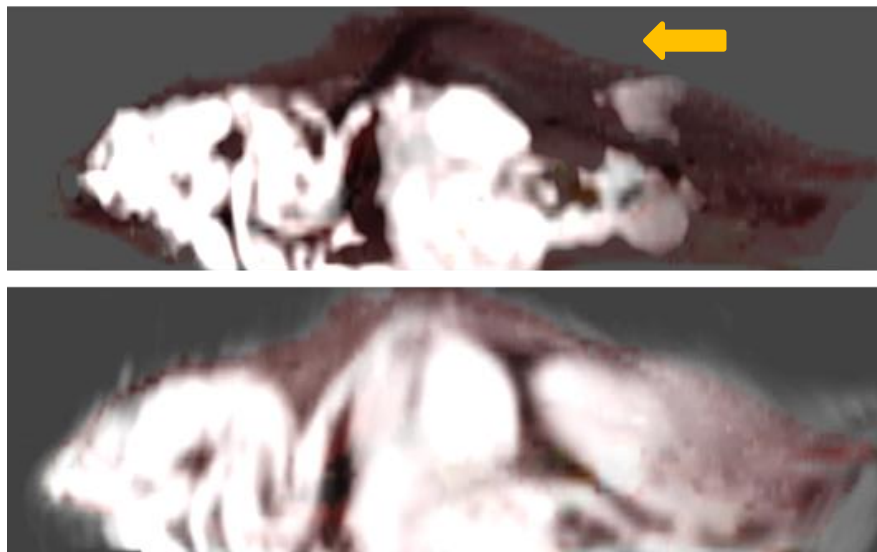
Figure 3.6: Overlay of an IDEAL water-separated MR image on top of the corresponding optical image in the sagittal plane following rigid registration (top) and non-rigid registration (bottom). The yellow arrow indicates a large region of misalignment in the rigid only registration along the back of the mouse. MR images are cropped to match the size of the optical volume.

Post-registration alignment in animals imaged alive can be seen in figures 3.6 and 3.7. Mean TRE values for animals imaged alive and post mortem are listed in table 3.1. Error values were lower in animals imaged post-mortem following both rigid and non-rigid components of the registration.
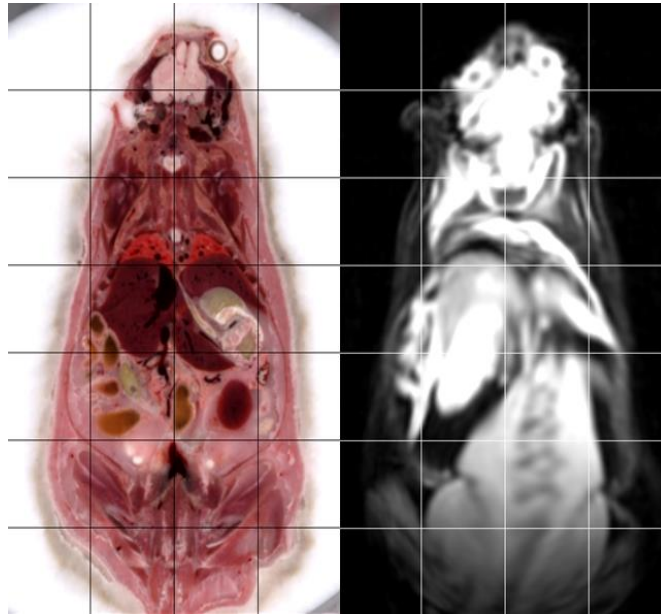
Figure 3.7: Coronal image of an optical volume (left) and corresponding post-registration water-separated IDEAL image (right) from a mouse in which MR images were acquired while the animal was still alive. The MR image is severely warped from the non-rigid registration and there is almost no correspondence can be seen between the two images.

Table 3.1
Mean (SD) TRE values from animals imaged alive and post-mortem following rigid and non-rigid registration

	Mean (SD) TRE (mm) Rigid	Mean (SD) TRE (mm) Non-rigid
MR Alive	5.99 (2.29)	5.53 (3.21)
MR Post-mortem	3.33 (2.23)	2.05 (1.42)
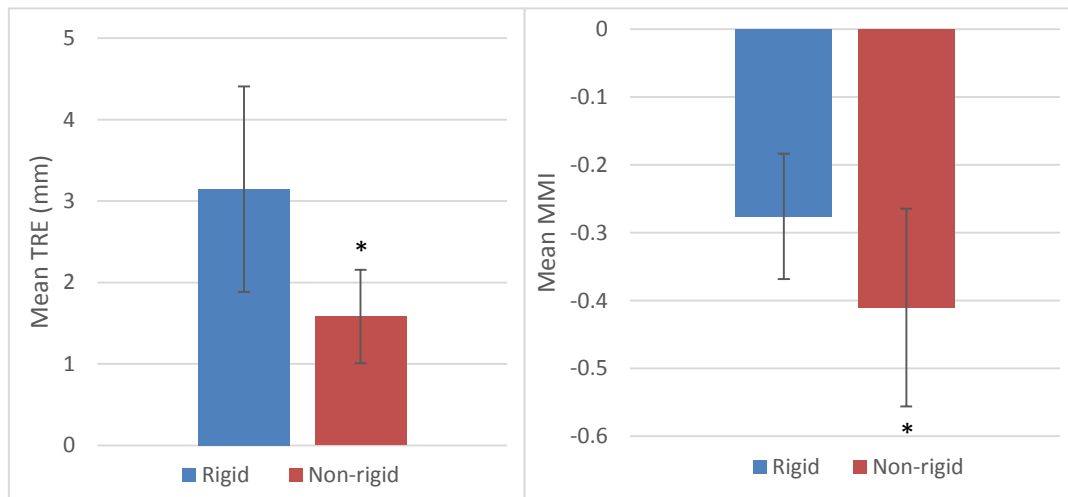
Figure 3.8: Mean TRE (left) and MMI (right) values before and after the non-rigid portion of the registration algorithm with error bars indicating standard deviation. Both the mean TRE and mean MMI values were significantly lower following non-rigid registration (P < 0.001). Values shown here were calculated from all registrations performed from mice imaged post-mortem.

Figure 3.8 compares mean TRE and MMI values before and after non-rigid registration from all registrations performed using images of mice acquired post-mortem. TRE and MMI decreased from 3.15 (1.26) to 1.58 (0.57) mm and -0.26 (0.11) to -0.41 (0.16) respectively which was determined to be significant ($P < 0.001$) in both cases.

Coronal, sagittal and axial planes of a single optical image co-registered with corresponding IDEAL, T1w and T2w MR contrasts can be seen in figure 3.9. Registrations utilizing T2w MR contrast had the lowest mean TRE of 1.23(0.62) mm. This value was determined to be significantly lower than both IDEAL and T1w TRE values ($P < 0.05$). Mean TRE values for IDEAL were the highest, however this failed to be significant compared with T1w TRE values ($P > 0.05$). Mean TRE and SD for each MR contrast following initialization, rigid, and non-rigid components of the registration algorithm are summarized in table 3.2. An example of MR and optical alignment following each portion of the registration is shown in figure 3.10. Relative error in each animal was consistent with mean values, as depicted in figure 3.11. In all but one case, the T2w weighted registration had the lowest mean TRE value and IDEAL had the highest.
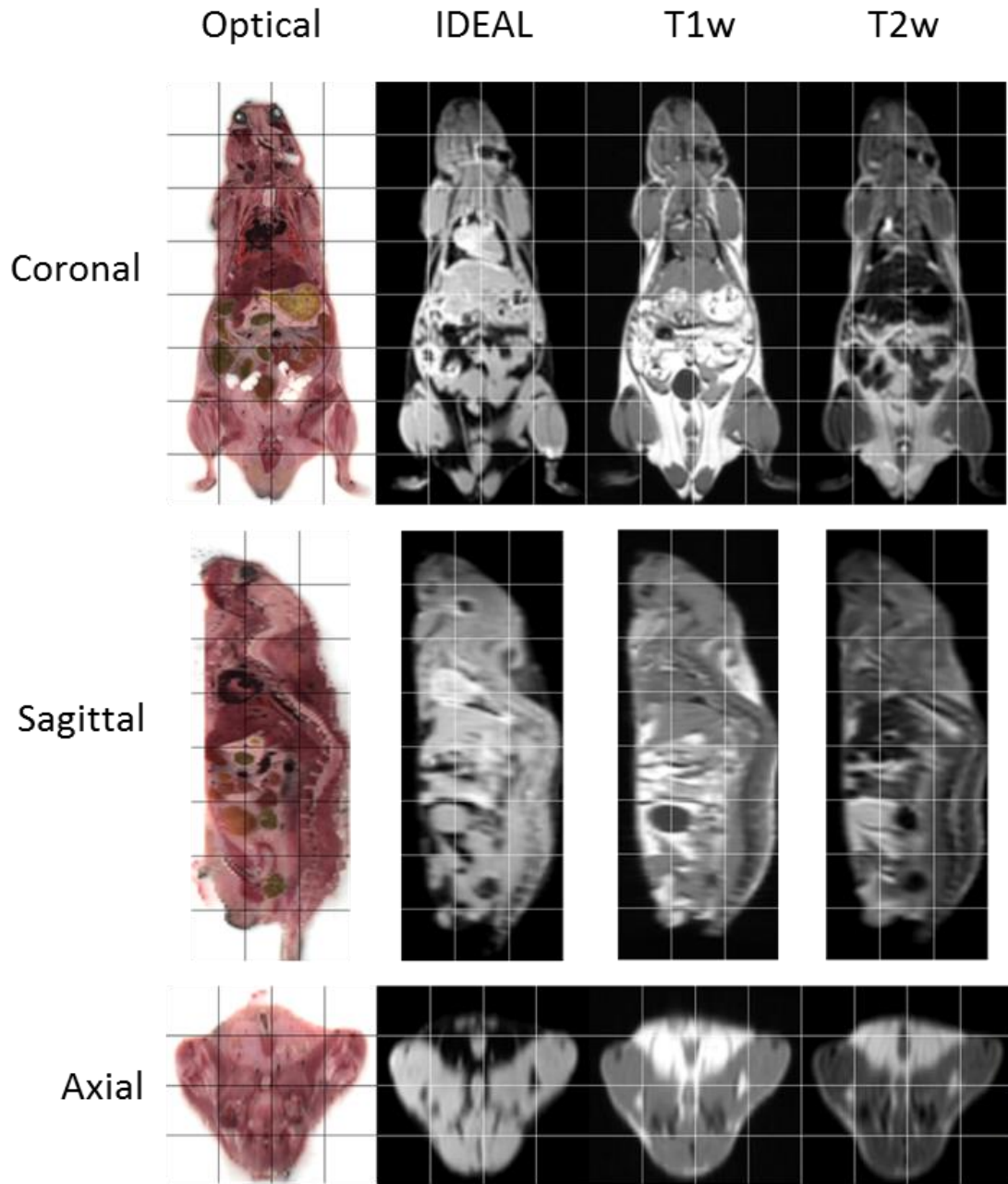
Figure 3.9: From top to bottom, coronal, sagittal and axial planes of optical images (left column) with corresponding post-registration T1w, T2w and water-separated MR images from left to right respectively; demonstrating anatomical agreement in all three planes following the proposed registration.

Table 3.2

Mean (SD) TRE values for MR contrasts following initialization, rigid and non-rigid portions of the registration

	Mean (SD) TRE (mm) Initialization	Mean (SD) TRE (mm) Rigid	Mean (SD) TRE (mm) B-Spline
IDEAL	8.05 (6.43)	3.33 (2.23)	2.05 (1.42)
T1w	9.43 (7.06)	3.24 (2.10)	1.48 (0.82)
T2w	8.81(7.10)	2.86(1.71)	1.23(0.62)

FLE on optical images was determined to be 0.27 mm, relative to the voxel size of approximately $0.02 \times 0.02 \times 0.2$ mm^3. FLE on MR images were 0.50 mm relative to voxel size $0.6 \times 0.6 \times 0.7$ mm^3 for T1w images, 0.47 mm relative to voxel size $0.8 \times 0.8 \times 0.7$ mm^3 for T2w images, and 0.59 mm relative to voxel size $0.9 \times 0.9 \times 0.7$ mm^3 for IDEAL images.
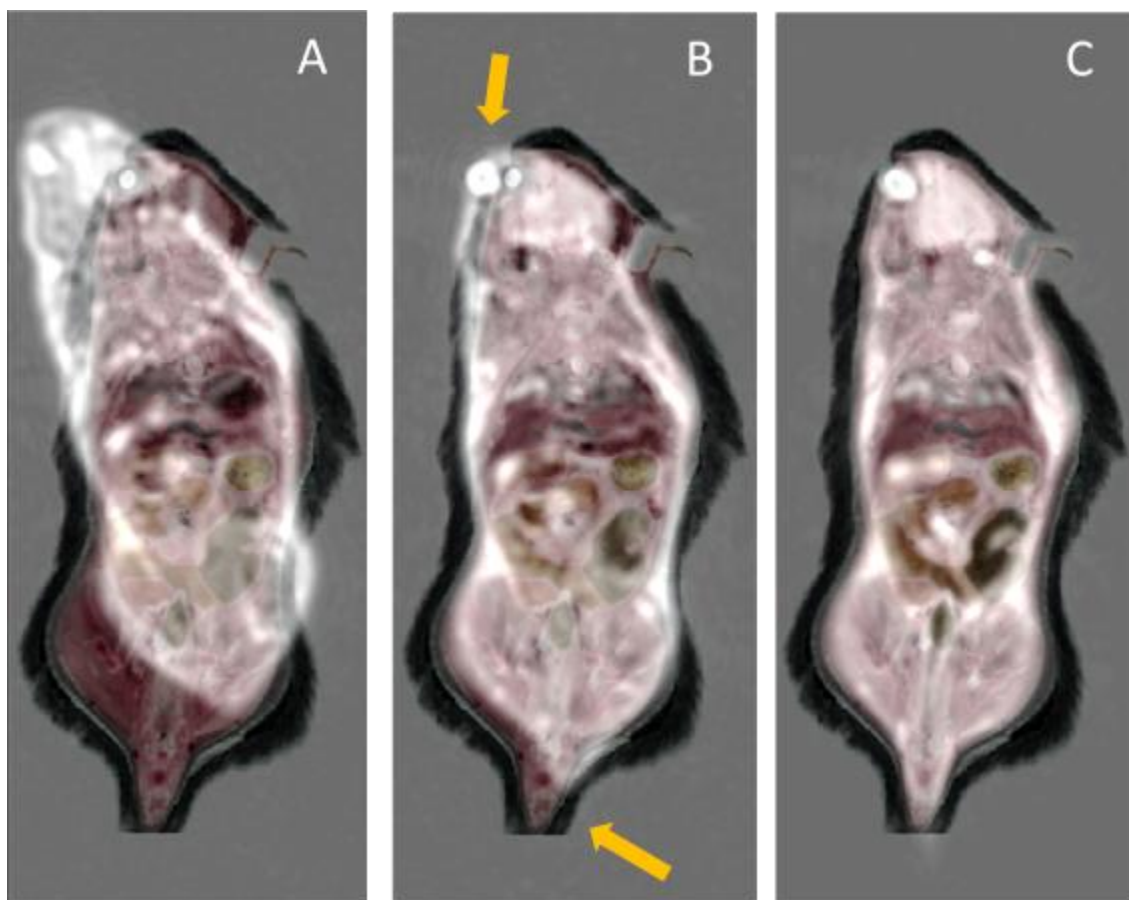
Figure 3.10: Overlays of a single optical image in the coronal plane with corresponding T2w MR images following (A) initialization, (B) rigid, and (C) non-rigid portions of the registration algorithm. Areas of obvious misalignment following rigid registration are indicated by the yellow arrows.
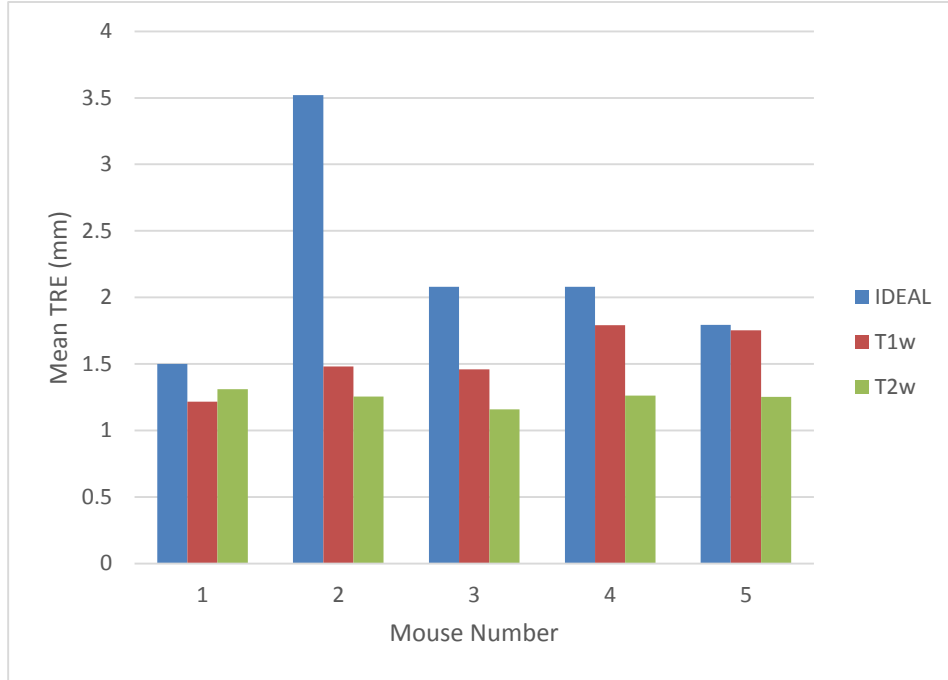
Figure 3.11: Mean TRE values for registrations using the different MR contrasts in each animal imaged showing the difference in alignment accuracy using different contrasts. In all but one case the T2w images had the lowest mean TRE values and IDEAL had the highest.

3.5 Discussion

In this study we proposed and validated a method for intensity based registration of 3D whole mouse optical and MR images volumes. As the first to investigate registration of these two image types over a whole mouse we explored a number of factors including image acquisition protocol, transformation types and different MR contrasts to determine their effect on registration accuracy.

Initially we investigated the effect of performing MR imaging before and after animal euthanasia. Qualitative comparison of post-registration anatomical agreement from animals imaged while still alive and those imaged post-mortem showed striking differences. In animals imaged while still alive, as seen in figure 3.6 in which the MR volume is overlaid on top of the optical, it can be seen that rigid registration (top) was able to align the volumes but there were areas of substantial misalignment, particularly along the dorsal surface of the animal indicated by the yellow arrow. Following the non-rigid component of registration (bottom) this volumetric misalignment was reduced. However, in an attempt to compensate for the deformations between images, the resulting post-registration MR volume is extremely warped and there is almost no anatomical agreement with the corresponding optical image (figure 3.7). Conversely, post-registration images from animals imaged post-mortem, seen in figure 3.9, show good anatomical agreement in all three planes. These observations were consistent with the associated mean TRE values displayed in table 1. The mean TRE following both the rigid and the non-rigid components of the registration are substantially lower for the images acquired when the animals were euthanized prior to MR image acquisition.

The relative success of registrations performed on volumes of animals imaged post-mortem can likely be attributed to the onset of rigor mortis during MR imaging in these mice. Because MR image acquisition required the animal remain immobile for approximately 1.5 hours following euthanasia to generate all three MR contrasts, the corpses naturally developed rigor mortis and became extremely stiff when being moved from the MR scanner and embedded within OCT and frozen; at which time their posture

was set for optical imaging. Due to this effect, tissue deformation between image modalities was substantially limited, reducing the required compensation from the registration process to align the volumes.

However, while imaging post-mortem was shown to substantially aid in registration by reducing deformation between imaging methods, it also increases the time between death and tissue fixation. Fixation during histological processing is done to stop the natural tissue degradation that occurs following death. This is done to maintain the *in vivo* biochemical and structural properties of the tissue as much as possible. As the degree of degradation is dependent on a number of processes including time[21], it is recommended that fixation is done immediately following euthanasia. Studies have shown however, that these effects may be delayed *in situ* compared to excised tissue[22] conventionally used for histological preparation. Moreover, during the first few hours post-mortem, which is relevant for this method, there may be minimal ultrastructural changes that occur[23]. Nevertheless, there will be some degree of tissue degradation that occurs using this approach and this may need to be taken into consideration and further investigated for different applications.

Post-mortem imaging also enabled the incorporation of a hair removal procedure prior to imaging. As the separation of hair from the underlying tissue in the optical images was a necessary step before registration using the proposed technique, a hair removal procedure was incorporated after the automated segmentations failed in two cases. This was done to

avoid manual segmentation which is not only time consuming but also susceptible to operator error. In the future, it would be desirable to reincorporate automated segmentation once it has been shown to be more reliable. This would substantially decrease the required time between euthanasia and tissue fixation and aid in limiting tissue degradation as previously described.

While performing all imaging post-mortem allowed for the degree of deformation between modalities to be substantially reduced, this approach was not able to warrant a rigid only approach. Examination of figure 3.10 showing an overlay of the two volumes at each step in the registration process demonstrates that following only the rigid portion of the registration there remain obvious regions of misalignment; some of which indicated by the yellow arrows. Subsequent non-rigid transformations, the result of which seen in figure 3.10 C, address these areas providing more accurate alignment.

Again, these observations are supported by the corresponding mean TRE values. For all contrasts, the difference between mean TRE values calculated before and after non-rigid registration was over 1mm. Moreover, this difference was determined to be significant using a pairwise t-test of the mean TRE values for each registered image pair (P < 0.001).

Similarly, the mean MMI value following the non-rigid portion of the registration was determined to be significantly lower than that following only the rigid transformation (P < 0.001). This is consistent with what we would expect as the larger negative value should

theoretically indicate a better alignment of the two images. This finding in conjunction with the significant reduction in mean TRE values suggests a relationship between the two measurements and supports the appropriateness of MMI as the metric for the current application.

Finally, we examined the effect of using different MR contrasts for registration. Utilization of the T2w MR contrast yielded the lowest mean TRE value of 1.23(0.62) mm, which falls within the distance of two MR voxels. Both T1w and IDEAL images were determined to have slightly higher mean TRE values, each falling within the distance of three of their respective MR voxels.

Calculated FLE values for each image type were small in relation to the TRE values and do not dominate the error measurement. In all of the MR contrasts the calculated FLE values are less than the size of a single voxel. The FLE value calculated for the optical images, while the smallest of all FLE values calculated, is large in relation to the optical voxel size. This is likely due to the relatively large anatomical features that were selected as landmarks, which was dictated by their visibility in the relatively low resolution MR images.

Despite the absolute difference in TRE values there may be little practical difference in the degree of accuracy achieved using the different MR contrasts. The anatomical agreement between the three different MR contrasts and the corresponding optical image

in all three planes can be seen in figure 3.9. From here it can be seen that all three MR images appear to be well aligned with the optical volume with little visible misalignment.

In conclusion, here we have proposed an intensity based method for registration of whole mouse optical and MR image volumes and explored its feasibility. Utilizing this approach along with T2w MR images a registration error of 1.23(0.62) mm was achieved, which is less than the size of two MR voxels. This work is the first to investigate registration of these two modalities over the area of a whole mouse. Combined with registration of whole mouse histological slides, this provides a promising method for registration of histology with *in vivo* MR images for tissues which become substantially deformed using more conventional histological processing techniques.

3.6 References

1.   Gao, Y.R., et al., *Validation of DTI Tractography-Based Measures of Primary Motor Area Connectivity in the Squirrel Monkey Brain.* Plos One, 2013. **8**(10).

2.   Zhan, Y.Q., et al., *Reqistering histologic and MR images of prostate for image-based cancer detection.* Academic Radiology, 2007. **14**(11): p. 1367-1381.

3.   Osechinskiy, S. and F. Kruggel, *Quantitative comparison of high-resolution MRI and myelin-stained histology of the human cerebral cortex.* 2009 Annual International Conference of the Ieee Engineering in Medicine and Biology Society, Vols 1-20, 2009: p. 85-89.

4.   Wang, H.J., et al., *Treatment of Rodent Liver Tumor With Combretastatin A4 Phosphate Noninvasive Therapeutic Evaluation Using Multiparametric Magnetic Resonance Imaging in Correlation With Microangiography and Histology.* Investigative Radiology, 2009. **44**(1): p. 44-53.

5.   Gibson, E., et al., *Registration of prostate histology images to ex vivo MR images via strand-shaped fiducials.* Journal of Magnetic Resonance Imaging, 2012. **36**(6): p. 1402-1412.

6.   Park, H., et al., *Registration methodology for histological sections and in vivo Imaging of human prostate.* Academic Radiology, 2008. **15**(8): p. 1027-1039.

7.   Choe, A.S., et al., *Accuracy of image registration between MRI and light microscopy in the ex vivo brain.* Magnetic Resonance Imaging, 2011. **29**(5): p. 683-692.

8.   Meyer, C.R., et al., *A methodology for registration of a histological slide and in vivo MRI volume based on optimizing mutual information.* Molecular Imaging, 2006. **5**(1): p. 16-23.

9.   Dauguet, J., et al., *Three-dimensional reconstruction of stained histological slices and 3D non-linear registration with in-vivo MRI for whole baboon brain.* Journal of Neuroscience Methods, 2007. **164**(1): p. 191-204.

10.   Yeh, W.C., et al., *Young's modulus measurements of human liver and correlation with pathological findings.* 2001 Ieee Ultrasonics Symposium Proceedings, Vols 1 and 2, 2001: p. 1233-1236.

11.   Comley, K. and N.A. Fleck, *A micromechanical model for the Young's modulus of adipose tissue.* International Journal of Solids and Structures, 2010. **47**(21): p. 2982-2990.

12.   Redig, A.J. and S.S. McAllister, *Breast cancer as a systemic disease: a view of metastasis.* Journal of Internal Medicine, 2013. **274**(2): p. 113-126.

13.   Weis, S.M. and D.A. Cheresh, *Tumor angiogenesis: molecular pathways and therapeutic targets.* Nat Med, 2011. **17**(11): p. 1359-70.

14.   Furukawa, S., et al., *Increased oxidative stress in obesity and its impact on metabolic syndrome.* J Clin Invest, 2004. **114**(12): p. 1752-61.

15.   Lavie, C.J., R.V. Milani, and H.O. Ventura, *Obesity and cardiovascular disease: risk factor, paradox, and impact of weight loss.* J Am Coll Cardiol, 2009. **53**(21): p. 1925-32.

16.   Rocha, V.Z. and E.J. Folco, *Inflammatory concepts of obesity.* Int J Inflam, 2011. **2011**: p. 529061.

17.   Gibson, E., *e.a.*, *3D Co-Registration of MRI and Histology in a Mouse Model of Obesity and Non-Alcoholic Fatty Liver Disease.* Proceedings of the International Society of Magnetic Resonance in Medicine, 2013. **21**: p. 3729.

18.   Roy, D., et al., *3D Cryo-Imaging: A Very High-Resolution View of the Whole Mouse.* Anatomical Record-Advances in Integrative Anatomy and Evolutionary Biology, 2009. **292**(3): p. 342-351.

19.   Mattes, D., et al., *PET-CT image registration in the chest using free-form deformations.* Ieee Transactions on Medical Imaging, 2003. **22**(1): p. 120-128.

20.   Fitzpatrick, J.M., J.B. West, and C.R. Maurer, *Predicting error in rigid-body point-based registration.* Ieee Transactions on Medical Imaging, 1998. **17**(5): p. 694-702.

21.   Campobasso, C.P., G. Di Vella, and F. Introna, *Factors affecting decomposition and Diptera colonization.* Forensic Sci Int, 2001. **120**(1-2): p. 18-27.

22.   Nunley, W.C., et al., *Delayed, in vivo hepatic post-mortem autolysis.* Virchows Arch B Cell Pathol, 1972. **11**(4): p. 289-302.

23.   Tomita, Y., et al., *Ultrastructural changes during in situ early postmortem autolysis in kidney, pancreas, liver, heart and skeletal muscle of rats.* Leg Med (Tokyo), 2004. **6**(1): p. 25-31.

Chapter 4 :

Conclusions and Future Work

4.1 Summary of Important Findings

Pathological evaluation of histology continues to play an important role in clinical diagnosis and staging of many conditions. This remains the case despite its many short comings. However development of novel MR imaging techniques offer a promising alternative to histology based diagnosis in many disease states, providing a non-invasive method to acquire images with a comprehensive view of the tissue of interest.

Incorporation of these imaging techniques into clinical practice relies on validation of MRI through direct correlation with the clinical gold-standard which is histology. This is ideally achieved through accurate registration of the two modalities.

Unfortunately, conventional histological preparation techniques require the tissue of interest be excised and processed individually; often leaving it substantially deformed in comparison with its former *in vivo* state. While some organs such as the brain and prostate can retain some of their structure observed *in vivo*, other organs like the liver lack this ability and become almost unrecognizably deformed during histological processing; making registration with *in vivo* images exceedingly difficult. Alternatively, histological processing can be performed on whole mice, eliminating the need for tissue to be excised. In doing this, deformation between *in vivo* images and histology can be substantially reduced, simplifying the necessary compensation required from registration to achieve accurate alignment.

Although whole mouse sectioning can substantially aid in registration, the task of aligning the two aforementioned modalities must also address differences in contrast, resolution and slice orientation. The latter possibly the most difficult to address as the problem is not merely that of finding the corresponding 2D MR slice for a given histology image. Rather, the histological image is most likely an oblique plane through multiple MR slices. A popular approach to addressing this problem, which we chose to utilize here, is the use of optical images acquired during sectioning which can be combined into a volume and used

as an intermediate image to aid registration and provide 3D context to acquired histological sections.

Using a previously developed manual technique[1] registration of whole mouse MR volumes and histology can be performed manually via co-registration with the optical volume intermediate. However, this approach requires manual selection of homologous anatomical features in each of the image types leaving it susceptible to operator introduced error. Registration of MRI and optical volumes is particularly difficult using this technique as a result of the substantial resolution and contrast changes between the two image types. Moreover, selection of unique anatomically homologous points becomes substantially more complicated with the addition of a third dimension. For these reasons, automation of co-registration between MRI and optical volumes was chosen as a priority and addressed in this work.

A number of different techniques and aspects of image registration were introduced in chapter 2. As a first attempt at registering these two image modalities over the volume of a whole mouse, an intensity based registration, optimizing mutual information was chosen for its ability to handle images acquired from different modalities.

A specific implementation of this type of registration was proposed in chapter 3 and validated using TRE measurements. In this study a protocol for imaging was proposed wherein all images used for registration were acquired post mortem allowing for rigor

mortis to set in between imaging sessions. As a result, deformation between image volumes was substantially reduced compared to MR images acquired while the animal was alive; enabling accurate alignment using the proposed method. It was also determined that while deformation had been substantially reduced by acquiring images post-mortem a rigid only transformation was not adequate to achieve the desirable degree of alignment and that additional non-rigid registration components were necessary. Finally, the performance of three different MR contrasts using the proposed registration was compared. Compared with T1w and IDEAL contrast images, T2w images were found to have significantly lower registration error. Furthermore, registration utilizing T2w MR images achieved a mean TRE value within two MR voxels supporting this approach as a feasible method for registering these two image types.

4.2 Future Work

4.2.1 Higher Resolution

The major limitation of the achievable accuracy in the current study is most likely the relatively low resolution of MR images used. Given the resolution of the MR images used, the achieved error value is likely nearing a minimum considering the effect of the associated FLE. Improving the resolution should allow for visibility of finer details in the MR images which could be used to refine alignment with the homologous features in the relatively high resolution optical images. Moreover, additional detail in MR images should improve the salience of a number of anatomical features visible in optical images. This would enable in the number landmarks chosen for TRE calculations to be increased;

providing more information about the accuracy of alignment. Additionally, localization of these points should improve with higher resolution images in turn decreasing FLE values.

Whether or not the proposed method would work with higher resolution MR images for input is unknown. However, should the registration fail to handle the higher resolution images in a desirable fashion the proposed method may still be usable as the initial component of a hierarchical registration. These methods use a "coarse-to-fine" strategy where some quality of the registration can be increased in complexity throughout the course of the registration[2]. For example, the proposed method used a rigid transform followed by two consecutive B-splines of increasing grid size which would be considered a hierarchical approach of increasing transform complexity. Similarly, resolution may be altered; starting at a low resolution and recovering anatomical detail as you move to higher resolution. These approaches have also shown large performance gains over approaches utilizing a single resolution or high density B-Spline[3]. Taking a hierarchical approach where images are down sampled to resolutions comparable to those validated here, and incorporating an additional step to further refine alignment using full resolution images may be an appropriate approach to incorporate higher resolution MR images into the existing framework proposed here.

4.2.2: Potential Applications

Now that the proposed approach has been validated, the next obvious step would be to use it as component of a research study. Considering the major advantage of this tool over conventional histological processing techniques is the ability to effectively retain a substantial amount of *in situ* tissue structure by eliminating the need to excise the tissue of interest for processing, the applications that would most benefit from this work would be those in which tissues become substantially deformed when excised.

During the development of this technique applications to obesity related diseases were of particular interest and motivated the inclusion of IDEAL contrast images in the current study. This category of conditions is related to an abnormal accumulation of lipid throughout the body and affects a number of tissues including the liver[4] and brown adipose tissue[5] both of which are extremely difficult to register when using conventional histological processing techniques

A specific application may be validation of liver lipid quantification using IDEAL as a diagnostic measure for staging of non-alcoholic fatty liver disease. This has a potential to improve upon the clinical gold standard currently based on evaluation of samples obtained through biopsy which have a tendency to misrepresent overall tissue properties due to their small sample size[6]. The obvious benefit of MR based diagnosis is the ability to view and quantify lipid content over the entire organ to make a more accurate assessment of lipid infiltration[7].

4.2.3: Additional Modalities

While the motivation behind choosing MRI as the *in vivo* imaging modality was explored in chapter 1, other imaging modalities could also be used to provide complementary information. In particular CT images can provide excellent contrast in bony structures and produce high resolution images in a fraction of the time of MRI. Considering the utility of MRI in soft tissue imaging, registration of these images with complimentary CT data has been previously identified and sought after in numerous applications[8]. Additionally,
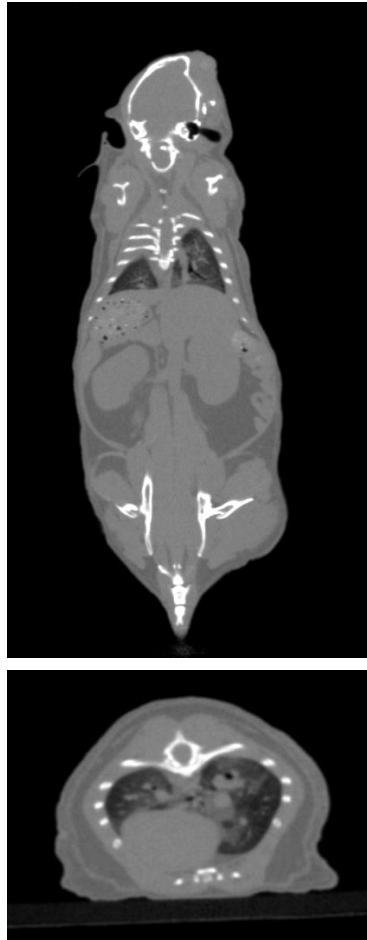
Figure 4.1: 3D CT image shown in coronal (top) and axial (bottom) planes acquired prior to MR imaging at 150μm resolution

CT is also an *in vivo* imaging modality and the same factors motivating the previously presented work would also apply; namely the use of histology as a validation tool.

In recent animals, CT imaging (performed by Jospeh Umoh) was incorporated into the current protocol both before MR imaging and following embedding and freezing of tissue in preparation for cryo-sectioning. These images can be acquired in less than 10 minutes with 150 micron isotropic resolution, an example of which is shown in figure 4.1. Hypothetically, images acquired of the frozen volume should require only a rigid transformation to achieve accurate alignment with optical images. An additional CT image was acquired prior to MR imaging in case the embedding media complicated the registration process.

At this point the ability of the proposed registration technique to register CT and optical image volumes has not been explored. While theoretically all components of this intensity based approach should be equally applicable to the CT images as the MR images, there are a number of parameters that will likely need to be optimized for this image type. Furthermore, because the CT images are at a substantially higher resolution than the MR images used in this study it may be appropriate to modify the approach and incorporate a hierarchical strategy as previously described in section 4.2.1. Nonetheless, co-registration of MR and CT volumes with the optical image volume would allow for all three modalities to be directly compared providing a wealth of complementary information to correlate and compare in different studies.

4.2.4: 2D Histology-Optical Co-registration

As discussed throughout this thesis, the main motivation behind this work was to eventually achieve full automation of registration between 3D whole mouse MR images and 2D histological sections. Registering MR and optical images is only half of the full registration in which a different transform will map histological sections to the appropriate plane of the optical volume as outlined in figure 1.5. Currently, combining the proposed method with the manual registration of histology to the optical volume[1], which has been demonstrated in figure 4.2, can achieve this. However for reasons previously mentioned manual registration is not optimal and in the future it would be advantageous to devise an approach to automate the registration of optical and histological images.
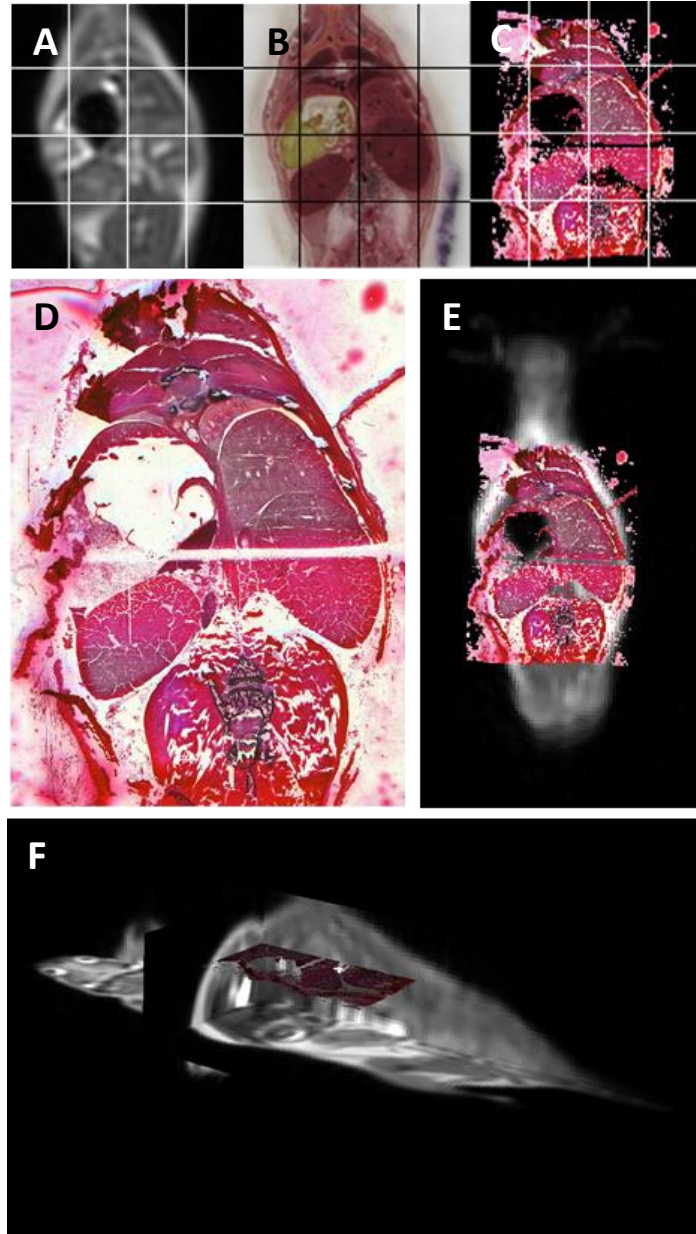
Figure 4.2: Example of co-registration between a histological section and 3D whole mouse T2w MR volume accomplished using a combination of the proposed method and manual registration. (D) Shows the original histological section prior to registration. Post registration overlays between the histological section and MRI can be seen in 2D coronal plane (E) and 3D (F). Anatomical correspondence can be seen between coronal sections of the (A) T2w MR image and (C) histology co-registered with the corresponding (B) optical image.

4.3 Conclusion

In this thesis I have presented a feasible method for accurately registering whole mouse 3D optical and MR image volumes automatically through an intensity based approach optimizing mutual information. After determining an appropriate imaging protocol in which all imaging is performed post-mortem, I validated the accuracy of the proposed method through calculation of TRE. Using these values the importance of the non-rigid component of the algorithm was confirmed. Furthermore, it was found that registrations utilizing T2w MR images had significantly lower registration error than either T1w or IDEAL contrast images.

Although this work was motivated by the desirability of MRI registration with histology, the utility of the registration as it currently stands should not be understated. Optical images are acquired with high resolution and are rich with contrast which can be used to assist in assessment of MR images. Moreover, inclusion of fluorescence filters in the optical imaging protocol can allow for a number of molecular processes to be investigated and correlated with MR images. However, as pathological tissue evaluation remains a common clinical gold-standard for diagnosis of many diseases the main purpose of this work is as a first step towards automated registration of whole mouse histological sections with 3D MR image volumes.

4.4 References

1.   Gibson, E., et al., *3D Co-Registration of MRI and Histology in a Mouse Model of Obesity and Non-Alcoholic Fatty Liver Disease.* Proceedings of the International Society of Magnetic Resonance in Medicine, 2013. **21**: 3729.

2.   Lester, H. and S.R. Arridge, *A survey of hierarchical non-linear medical image registration.* Pattern Recognition, 1999. **32**(1): p. 129-149.

3.   Lee, S., G. Wolberg, and S.Y. Shin, *Scattered data interpolation with multilevel B-splines.* Ieee Transactions on Visualization and Computer Graphics, 1997. **3**(3): p. 228-244.

4.   Lewis, J.R. and S.R. Mohanty, *Nonalcoholic Fatty Liver Disease: A Review and Update.* Digestive Diseases and Sciences, 2010. **55**(3): p. 560-578.

5.   Loyd, C. and S. Obici, *Brown fat fuel use and regulation of energy homeostasis.* Curr Opin Clin Nutr Metab Care, 2014. **17**(4): p. 368-72.

6.   Ratziu, V., et al., *Sampling variability of liver biopsy in nonalcoholic fatty liver disease.* Gastroenterology, 2005. **128**(7): p. 1898-906.

7.   Liu, C.Y., et al., *Fat quantification with IDEAL gradient echo imaging: correction of bias from T(1) and noise.* Magn Reson Med, 2007. **58**(2): p. 354-64.

8.   Maintz, J.B. and M.A. Viergever, *A survey of medical image registration.* Med Image Anal, 1998. **2**(1): p. 1-36.

Appendix A: Registration Code

```cpp
// BY: Jacqueline K Harris
// 3D Whole Mouse MRI and Optical image volume registration
//
// Code is designed to perform a non-rigid 3D registration of a
// MRI volume to a corresponding 3D whole mouse optical volume.
//
// INPUTS:
//    -A 3D RGB Block Face NIfTI file
//    -A 3D MRI NIfTI file
// OUTPUTS:
//    -A 3D transformed MRI NIfTI file following rigid, coarse B-
//     spline and fine B-spline components of registration
//    -Transforms for rigid, coarse B-spline and fine B-spline
//     used to align volumes

#include <iostream>
using namespace std;

//ITK header files
#include "itkImage.h"
#include "itkRGBPixel.h"
#include "itkImageFileReader.h"
#include "itkImageFileWriter.h"
#include "itkRGBToLuminanceImageFilter.h"
#include "itkChangeInformationImageFilter.h"
#include "itkCenteredTransformInitializer.h"
#include "itkImageRegistrationMethod.h"
#include "itkMattesMutualInformationImageToImageMetric.h"
#include "itkVersorRigid3DTransform.h"
#include "itkVersorRigid3DTransformOptimizer.h"
#include "itkResampleImageFilter.h"
#include "itkTransformFileWriter.h"
#include "itkTransformFileReader.h"
#include "itkTransformFactoryBase.h"
#include "itkImageRegistrationMethod.h"


#include "itkCenteredTransformInitializer.h"
#include "itkMattesMutualInformationImageToImageMetric.h"
#include "itkVersorRigid3DTransform.h"
```

```cpp
#include "itkVersorRigid3DTransformOptimizer.h"

#include "itkBSplineDeformableTransform.h"

//#include "reg.h"
typedef itk::Image<double, 3> ImageType;
ImageType::Pointer CenterVolume(string, ImageType::Pointer);
int RigidReg(string, string, string, string);
void BSpline(string, string, string, string, int, int, int,
int);
void TRE(int, double, double, double, double, double, double,
string);


int main() {

    clock_t start;
   double duration;

   start = std::clock();

    string path =
    "C:\\Users\\Jacqueline\\Documents\\Jackie\\ITK\\Volumes\\Ju
    ly182013\\";
    string date = "July182013";
    string MR = "MRT2w";
    string ext = "";
    string tag = "";

    string Input_BlockFace = path + "BlockFace_" + date + ext +
    ".nii";
    string Input_MR = path + MR + "_" + date + ".nii";
    string Output_Image = path + "Output_" + MR + "_Rigid_" +
    date + ext + tag + ".nii";
    string Output_Transform = path + "Output_Transform_Rigid" +
    MR + "_" + date + ext + tag + ".tfm";

    string Output_CenteredBlockFace = path +
    "Centered_BlockfaceInput_" + date + ext + tag + ".nii";
    string Output_CenteredMR = path + MR + "_Input_" + date +
    ext +  tag + ".nii";

    string OutputRigidImage = path + "Output_" + MR + "_Rigid_"
    + date + ext + tag + ".nii";
```

```cpp
string OutputRigidTransform = path +
"Output_Transform_Rigid" + MR + "_" + date + ext + tag +
".tfm";

string OutputCoarseBSplineImage = path + "Output_" + MR +
"_BSpline_" + date + ext + tag + ".nii";
string OutputCoarseBSplineTransform = path +
"Output_BSplineTransform_" + MR + "_" + date + ext + tag +
".tfm";

string OutputFineBSplineImage = path + "Output_" + MR +
"_Fine_" + date + ext + tag + ".nii";
string OutputFineBSplineTransform = path +
"Output_FineTransform_" + MR + "_" + date + ext + tag +
".tfm";

// -------------Type definitions-------------
typedef itk::RGBPixel<unsigned char> ColorPixelType;
typedef itk::Image<ColorPixelType, 3> ColorImageType;
typedef itk::ImageFileReader<ColorImageType>
ColorReaderType;
typedef itk::ImageFileReader<ImageType> MRReaderType;

// Read/Write
ColorReaderType::Pointer ColorImageReader =
ColorReaderType::New();
ColorImageReader->SetFileName(Input_BlockFace);
MRReaderType::Pointer MRImageReader = MRReaderType::New();
MRImageReader->SetFileName(Input_MR);
ColorImageReader->Update();
std::cout << "Done Read" << std::endl;

// Luminance Filter For Fixed Image
typedef itk::RGBToLuminanceImageFilter<ColorImageType,
ImageType> LuminanceFilterType;
LuminanceFilterType::Pointer LuminanceFilter =
LuminanceFilterType::New();
LuminanceFilter->SetInput(ColorImageReader->GetOutput());

ImageType* FixedImage = LuminanceFilter->GetOutput();
ImageType* MovingImage = MRImageReader->GetOutput();

FixedImage = CenterVolume(Output_CenteredBlockFace,
FixedImage);
MovingImage = CenterVolume(Output_CenteredMR, MovingImage);
std::cout << "Done Center" << std::endl;
```

```cpp
        RigidReg(Output_CenteredBlockFace, Output_CenteredMR,
        OutputRigidImage, OutputRigidTransform);

        int XNumNodes = 3;
        int YNumNodes = 2;
        int ZNumNodes = 5;
        int minStep = 0.001;

        BSpline(OutputCoarseBSplineImage,
        OutputCoarseBSplineTransform, Output_CenteredBlockFace,
        OutputRigidImage, XNumNodes, YNumNodes, ZNumNodes,
        minStep);

        XNumNodes = 7;
        YNumNodes = 5;
        ZNumNodes = 10;
        minStep = 0.0001;

        BSpline(OutputFineBSplineImage, OutputFineBSplineTransform,
        Output_CenteredBlockFace, OutputCoarseBSplineImage,
        XNumNodes, YNumNodes, ZNumNodes, minStep);

        duration = ( std::clock() - start ) / (double)
        CLOCKS_PER_SEC;
        cout<<"Total Registration Time: "<< duration <<'\n';


}

ImageType::Pointer CenterVolume(string OutputFile,
ImageType::Pointer Image) {

        typedef itk::ChangeInformationImageFilter<ImageType>
        CenterFilterType;
        CenterFilterType::Pointer CenterFilter =
        CenterFilterType::New();
        CenterFilter->SetInput(Image);
        CenterFilter->CenterImageOn();

        if (!OutputFile.empty()){
                typedef itk::ImageFileWriter<ImageType> WriterType;
                WriterType::Pointer Writer = WriterType::New();
                Writer->SetFileName(OutputFile);
                Writer->SetInput(CenterFilter->GetOutput());
                Writer->Update();
```

```cpp
        }

        return Image;
}

int RigidReg(string FixedFile, string MovingFile, string
OutputImageFile, string OutputTransFile) {

        clock_t start;
        double duration;

        start = std::clock();

        double numHistBin = 50;

        // -------------Type definitions-------------

        //Image
        typedef itk::Image<double, 3> ImageType;
        typedef itk::ImageFileReader<ImageType> MovingReaderType;
        typedef itk::ImageFileWriter<ImageType> WriterType;
        typedef itk::ImageFileReader<ImageType> FixedReaderType;


        //Registration
        typedef itk::VersorRigid3DTransform<double> TransformType;
        typedef itk::VersorRigid3DTransformOptimizer OptimizerType;
        typedef
        itk::MattesMutualInformationImageToImageMetric<ImageType,
        ImageType> MetricType;
        typedef itk::LinearInterpolateImageFunction<ImageType,
        double> InterpolatorType;
        typedef itk::ImageRegistrationMethod<ImageType, ImageType>
        RegistrationType;
        typedef itk::CenteredTransformInitializer<TransformType,
        ImageType, ImageType> InitializerType;
        typedef TransformType::VersorType VersorType;
        typedef VersorType::VectorType VectorType;
        typedef OptimizerType::ScalesType OptimizerScalesType;

        //Resample
        typedef itk::ResampleImageFilter<ImageType, ImageType>
        ResamplerType;

        //------------Pointers------------
        // Read/Write
```

```
FixedReaderType::Pointer FixedImageReader =
FixedReaderType::New();
MovingReaderType::Pointer MovingImageReader =
MovingReaderType::New();
WriterType::Pointer Writer = WriterType::New();
FixedImageReader->SetFileName(FixedFile);
MovingImageReader->SetFileName(MovingFile);
Writer->SetFileName(OutputImageFile);
FixedImageReader->Update();

//Registration compenents
MetricType::Pointer Metric = MetricType::New();
OptimizerType::Pointer Optimizer = OptimizerType::New();
InterpolatorType::Pointer Interpolator =
InterpolatorType::New();
RegistrationType::Pointer Registration =
RegistrationType::New();
TransformType::Pointer Transform = TransformType::New();
InitializerType::Pointer Initializer =
InitializerType::New();


//----------Registration----------
//Connect cregistration components
Registration->SetMetric(Metric);
Registration->SetOptimizer(Optimizer);
Registration->SetInterpolator(Interpolator);
Registration->SetTransform(Transform);
Registration->SetMovingImage(MovingImageReader-
>GetOutput());
Registration->SetFixedImage(FixedImageReader->GetOutput());

//FixedImageReader->Update();
Registration->SetFixedImageRegion(FixedImageReader-
>GetOutput()->GetBufferedRegion());
Registration->SetInitialTransformParameters(Transform-
>GetParameters());

//Metric Parameters
Metric->SetNumberOfHistogramBins(numHistBin);
Metric->UseAllPixelsOn();
Metric->ReinitializeSeed( 76926294 );

//Initializer
Initializer->SetTransform(Transform);
```

```cpp
Initializer->SetMovingImage(MovingImageReader-
>GetOutput());
Initializer->SetFixedImage(FixedImageReader->GetOutput());
Initializer->MomentsOn();
Initializer->InitializeTransform();

//Versor
VersorType Rotation;
VectorType Axis;
Axis[0] = 0.0;
Axis[1] = 0.0;
Axis[2] = 1.0;
const double Angle = 0;
Rotation.Set(Axis, Angle);
Transform->SetRotation(Rotation);

//Optimizer
OptimizerScalesType optimizerScales(Transform-
>GetNumberOfParameters());
const double translationScale = 1.0/10000;
optimizerScales[0] = 1.0;
optimizerScales[1] = 1.0;
optimizerScales[2] = 1.0;
optimizerScales[3] = translationScale;
optimizerScales[4] = translationScale;
optimizerScales[5] = translationScale;
Optimizer->SetScales(optimizerScales);
Optimizer->SetMaximumStepLength(4.000);
Optimizer->SetMinimumStepLength(0.05);
Optimizer->SetNumberOfIterations(200);

//Do Registration
Registration->Update();

//Get Output
OptimizerType::ParametersType FinalParameters =
Registration->GetLastTransformParameters();
const double versorX = FinalParameters[0];
const double versorY = FinalParameters[1];
const double versorZ = FinalParameters[2];
const double finalTranslationX = FinalParameters[3];
const double finalTranslationY = FinalParameters[4];
const double finalTranslationZ = FinalParameters[5];
const unsigned int numberOfIterations = Optimizer-
>GetCurrentIteration();
const double bestValue = Optimizer->GetValue();
```

```cpp
//Print Results
std::cout << std::endl << std::endl;
std::cout << "Result = " << std::endl;
std::cout << " Versor X       = " <<versorX << std::endl;
std::cout << " Versor Y       = " <<versorY << std::endl;
std::cout << " Versor Z       = " <<versorZ << std::endl;
std::cout << " Translation X = " <<finalTranslationX <<
std::endl;
std::cout << " Translation Y = " <<finalTranslationY <<
std::endl;
std::cout << " Translation Z = " <<finalTranslationZ <<
std::endl;
std::cout << " Iterations     = " << numberOfIterations <<
std::endl;
std::cout << " Metric Value  = " << bestValue << std::endl;

//Resample moving image to transformed image for output
ResamplerType::Pointer Resampler = ResamplerType::New();
Resampler->SetTransform(Transform);
Resampler->SetOutputParametersFromImage(FixedImageReader-
>GetOutput());
Resampler->SetInput(MovingImageReader->GetOutput());

//Write
Writer->SetInput(Resampler->GetOutput());
Writer->Update();

//Write Transform
itk::TransformFileWriter::Pointer writer =
itk::TransformFileWriter::New();
writer->SetInput(Transform);
writer->SetFileName(OutputTransFile);
writer->Update();

//------Transform Test------
string fileName;
fileName = OutputTransFile;

// Register default transforms
itk::TransformFactoryBase::RegisterDefaultTransforms();

itk::TransformFileReader::Pointer reader =
itk::TransformFileReader::New();
reader->SetFileName(fileName);
reader->Update();
```

```cpp
        // Display the transform
        std::cout << *(reader->GetTransformList()->begin()) <<
        std::endl;

        duration = ( std::clock() - start ) / (double)
        CLOCKS_PER_SEC;
        cout<<"Rigid Registration Time: "<< duration <<'\n';

        return 0;
}

void BSpline(string OutputImageFile, string OutputTransformFile,
string FixedImageFile, string MovingImage, int numNodesX, int
numNodesY, int numNodesZ, int minStep) {

        clock_t start;
        double duration;

        start = std::clock();

        int maxStep = 4;

        const int ImageDim = 3;
        typedef short PixelType;

        // TYPE DEFINITIONS
        typedef itk::Image<short, 3> ImageType;
        typedef itk::ImageFileReader<ImageType> ReaderType;
        typedef
        itk::MattesMutualInformationImageToImageMetric<ImageType,
        ImageType> MetricType;
        typedef itk::LinearInterpolateImageFunction<ImageType>
        InterpolatorType;
        typedef itk::RegularStepGradientDescentOptimizer
        OptimizerType;
        typedef itk::BSplineDeformableTransform<double, 3, 3>
        TransformType;
        typedef itk::ImageRegistrationMethod<ImageType, ImageType>
        RegistrationType;
        typedef itk::ResampleImageFilter<ImageType,ImageType>
        ResamplerType;
        typedef itk::ImageFileWriter<ImageType> WriterType;
        std::cout << "Done Type Defs" << std::endl;

        // OBJECT CREATION
```

```
ReaderType::Pointer FixedImageReader = ReaderType::New();
FixedImageReader->SetFileName(FixedImageFile);
ImageType::ConstPointer FixedImage = FixedImageReader-
>GetOutput();
FixedImageReader->Update();

ReaderType::Pointer MovingImageReader = ReaderType::New();
MovingImageReader->SetFileName(MovingImage);
MovingImageReader->Update();

WriterType::Pointer Writer = WriterType::New();
Writer->SetFileName(OutputImageFile);

RegistrationType::Pointer Registration =
RegistrationType::New();
std::cout << "Done Object Creation" << std::endl;

//Connect Registration Components
OptimizerType::Pointer Optimizer = OptimizerType::New();
TransformType::Pointer Transform = TransformType::New();
MetricType::Pointer Metric = MetricType::New();
InterpolatorType::Pointer Interpolator =
InterpolatorType::New();
ResamplerType::Pointer Resample = ResamplerType::New();
std::cout << "Done Connecting" << std::endl;

//Get Image Parameters
ImageType::SpacingType FixedSpacing = FixedImage-
>GetSpacing();
ImageType::SizeType FixedSize =
FixedImage->GetLargestPossibleRegion().GetSize();
ImageType::PointType FixedOrigin = FixedImage->GetOrigin();
ImageType::DirectionType FixedDirection = FixedImage-
>GetDirection();

std::cout << "Size ";
std::cout << FixedSize[0] << ", " << FixedSize[1] << ", "
<< FixedSize[2] << std::endl;

std::cout << "Origin ";
std::cout << FixedOrigin[0] << ", " << FixedOrigin[1] << ",
" << FixedOrigin[2] << std::endl;

std::cout << "Spacing ";
```

```cpp
      std::cout << FixedSpacing[0] << ", " <<
      FixedSpacing[1] << ", " << FixedSpacing[2] <<
      std::endl;

  // PARAMETER TUNING

  // Number of Nodes
  TransformType::SizeType GridSize;
  GridSize[0] = numNodesX + 3;
  GridSize[1] = numNodesY + 3;
  GridSize[2] = numNodesZ + 3;
  TransformType::RegionType BSplineRegion;
  BSplineRegion.SetSize(GridSize);
  Transform->SetGridRegion(BSplineRegion);

  // Node Spacing
  TransformType::SpacingType Spacing;
  Spacing[0] = FixedSize[0]*FixedSpacing[0] / numNodesX;
  Spacing[1] = FixedSize[1]*FixedSpacing[1] / numNodesY;
  Spacing[2] = FixedSize[2]*FixedSpacing[2] / numNodesZ;
  Transform->SetGridSpacing(Spacing);

  std::cout << "Grid Spacing ";
  std::cout << Spacing[0] << ", " << Spacing[1] << ", " <<
  Spacing[2] << std::endl;

  // Set origin
  TransformType::OriginType Origin;
  Origin[0] = (abs(FixedOrigin[0]) * -1) - Spacing[0];
  Origin[1] = (abs(FixedOrigin[1]) * -1) - Spacing[1];
  Origin[2] = (abs(FixedOrigin[2]) * -1) - Spacing[2];
  Transform->SetGridOrigin(Origin);

  // Registration
  RegistrationType::ParametersType
  InitialParameters(GridSize[0]*GridSize[1]*GridSize[2]*3);
  InitialParameters.Fill(0.0);
  Registration->SetInitialTransformParameters
  (InitialParameters);

  //Metric Parameters
  Metric->SetNumberOfHistogramBins(50);

  // Set step sizes
  Optimizer->SetMaximumStepLength(maxStep);
  Optimizer->SetMinimumStepLength(minStep);
```

```cpp
        std::cout << "Done Parameters" << std::endl;

        // PIPELINE CONNECTION
        Registration->SetFixedImage(FixedImage);
        Registration->SetMovingImage(MovingImageReader-
>GetOutput());
        Registration->SetMetric(Metric);
        Registration->SetOptimizer(Optimizer);
        Registration->SetTransform(Transform);
        Registration->SetInterpolator(Interpolator);
        std::cout << "Done Connecting Pipeline" << std::endl;

        // ACTION!
        std::cout << "Start Registration" << std::endl;
        Registration->Update();
        std::cout << "Done Registration" << std::endl;

        // PROVIDING OUTPUT TO THE USER
        Resample->SetTransform(Transform);
        Resample->SetOutputParametersFromImage(FixedImage);
        Resample->SetInput(MovingImageReader->GetOutput());
        Writer->SetInput(Resample->GetOutput());

        typedef itk::TransformFileWriter TransformWriterType;
        TransformWriterType::Pointer transformWriter =
        TransformWriterType::New();
        transformWriter->AddTransform(Transform);
        transformWriter->SetFileName(OutputTransformFile);
        transformWriter->Update();

        Writer->Update();

        duration = ( std::clock() - start ) / (double)
        CLOCKS_PER_SEC;
        cout<<"BSpline Registration Time: "<< duration <<'\n';

        const double bestValue = Optimizer->GetValue();
        std::cout << " Metric Value  = " << bestValue << std::endl;

}
```

Appendix B: Ethics Approval

Western

AUP Number: 2011-055
PI Name: McKenzie, Charles
AUP Title: Molecular and Metabolic MRI of Non-Alcoholic Fatty Liver Disease
Approval Date: 11/15/2011

Official Notice of Animal Use Subcommittee (AUS) Approval: Your new Animal Use Protocol (AUP) entitled " Molecular and Metabolic MRI of Non-Alcoholic Fatty Liver Disease" has been APPROVED by the Animal Use Subcommittee of the University Council on Animal Care. This approval, although valid for four years, and is subject to annual Protocol Renewal.2011-055::1

1. This AUP number must be indicated when ordering animals for this project.
2. Animals for other projects may not be ordered under this AUP number.
3. Purchases of animals other than through this system must be cleared through the ACVS office. Health certificates will be required.

The holder of this Animal Use Protocol is responsible to ensure that all associated safety components (biosafety, radiation safety, general laboratory safety) comply with institutional safety standards and have received all necessary approvals. Please consult directly with your institutional safety officers.

Submitted by: Copeman, Laura
on behalf of the Animal Use Subcommittee
University Council on Animal Care

Curriculum Vitae

Jacqueline Harris

<u>**Education**</u>

09/ 12 – 09/14 University of Western Ontario, London ON
M.Sc. Candidate Medical Biophysics
Supervisor: Dr. Charles McKenzie

09/ 07 – 06/12 Queen's University, Kingston ON
B.Sc. (Honours) Major in Life Science
Science Minor Computer and Information Science

<u>**Research Experience**</u>

05/11 - 08/11 **Undergraduate Research Assistant**
Dr. Michael Colicos
Hotchkiss Brain Institute
University of Calgary, Calgary AB
Research focus: Analysis of changes in neuronal firing pattern resulting from different stimulation frequencies

02/11 – 04/11 **Undergraduate Research Assistant**
Dr. Ken Rose
Biomedical and Molecular Science,
Queen's University, Kingston ON
Research focus: Expanding upon existing neuronal simulating software

05/ 10 – 08/10 **Undergraduate Research Assistant**
Dr. Michael Colicos
Hotchkiss Brain Institute
University of Calgary, Calgary AB
Research focus: Studying the effects of folic acid fortification on developing neuronal networks

<u>**Peer reviewed Publications**</u>
Published or In Press

1. Girotto, F., Scott, L., Avchalumov, Y., **Harris, J.,** Iannattone, S., Drummond-Main, C., Tobias R., Bello-Espinosa L., Rho J. M., Davidsen J., Teskey G. C., Colicos, M. A. (2013). High dose folic acid supplementation of rats alters synaptic transmission and seizure susceptibility in offspring. *Scientific Reports, 3*. doi: Artn 1465.

Conference Proceedings

1. Colin M McCurdy, Bryan T Addeman, Curtis N Wiens, Lanette J Friesen-Waldner, Trevor P Wade, **Jacqueline K Harris**, Abraam S Soliman, Kevin J Sinclair, Charles A McKenzie, Automated Volumetric Fat Quantification of Adipose Tissue in Mice, Proceedings of the International Society of Magnetic Resonance in Medicine, 2014.

2. Friesen-Waldner L.J., Wade T.P., Wiens C.N., Thind K., **Harris J.K.**, Sinclair K.J., McCurdy C.M., Chen A.P., Borradaile N., McKenzie C.A., Hyperpolarised [1-13C]-Pyruvate Metabolism in Brown Fat, Proceedings of the International Society of Magnetic Resonance in Medicine, 2013.

3. Gibson E., Friesen-Waldner L., Hamilton A., Ribot E., Wade T.P., Wiens C.N., Thind K., **Harris J.**, Borradaile N., McKenzie C.A., Ward A., 3D Co-Registration of MRI and Histology in a Mouse Model of Obesity and Non-Alcoholic Fatty Liver Disease, Proceedings of the International Society of Magnetic Resonance in Medicine, 2013.

Peer Reviewed Presentations

1. **Harris J.,** Gibson E., Friesen-Waldner L., Hamilton A., Ribot E., Wade T., Wiens C., Thind K., Borradaile N., Ward A.., McKenzie C., Mutual Information Based 3D Rigid Registraion of Optical Whole Mouse and MR Images, Poster Presentation at the 2014 Imaging Network Ontario Symposium, Toronto ON, March 2014.

2. Colin M McCurdy, Bryan T Addeman, Curtis N Wiens, Lanette J Friesen-Waldner, Trevor P Wade, **Jacqueline K Harris**, Abraam S Soliman, Kevin J Sinclair, Charles A McKenzie, Automated Volumetric Fat Quantification of Adipose Tissue in Mice, Poster Presentation at the 2014 Imaging Network Ontario Symposium, Toronto ON, March 2014.

3. **Harris J.,** Gibson E., Friesen-Waldner L., Hamilton A., Ribot E., Wade T., Wiens C., Thind K., Borradaile N., Ward A., McKenzie C., Mutual Information Based 3D Rigid Registraion of Optical Whole Mouse and MR Images, Poster Presentation at the 2014 London Health Research Day, London ON, March 2014.

4. Colin M McCurdy, Bryan T Addeman, Curtis N Wiens, Lanette J Friesen-Waldner, Trevor P Wade, **Jacqueline K Harris**, Abraam S Soliman, Kevin J Sinclair, Charles A McKenzie, Automated Volumetric Fat Quantification of Adipose Tissue in Mice, Poster Presentation at the 2014 London Health Research Day, London ON, March 2014.

5. **Harris J.,** Gibson E., Hamilton A., McCurdy C., Friesen-Waldner L., Ward A.., McKenzie C., Feasibility of Brown Adipose Tissue Histology Co-registration with

3D Whole Mouse MR Images, Poster Presentation at the NIH Conference: Exploring the Role of Brown Fat in Humans, Bethesda MD, February 2014.

6. McCurdy C., Addeman B., Wiens C., Friesen-Waldner L., Wade T., **Harris J.,** Soliman A., Sinclair K., McKenzie C., Interscapular rown Adipose Tissue and Adipose Distribution in Magnetic Resonance Images of Mice, Poster Presentation at the NIH Conference: Exploring the Role of Brown Fat in Humans, Bethesda MD, February 2014.

7. **Harris J.,** Gibson E., Friesen-Waldner L., Hamilton A., Ribot E., Wade T., Wiens C., Thind K., Borradaile N., Ward A.., McKenzie C., Mutual Information Based 3D Rigid Registraion of Optical Whole Mouse and MR Images, Poster Presentation at the London Imaging Discovery Forum, London ON, June 2013.

8. Friesen-Waldner L.J., Wade T.P., Wiens C.N., Thind K., **Harris J.K**., Sinclair K.J., McCurdy C.M., Chen A.P., Borradaile N., McKenzie C.A., Hyperpolarised [1-13C]-Pyruvate Metabolism in Brown Fat, Poster Presentation at the 2013 Imaging Network Ontario Symposium, Toronto ON, February 2013.

Honours and Awards

09/13 – 09/14 **Ontario Graduate Scholarship**
Ontario Ministry of Training, Colleges and Universities

09/12 – 09/14 **Western Graduate Research Scholarship**
The University of Western Ontario, London ON

01/12 – 04/12 **Dean's Special Awards - Faculty of Arts and Science**
Queen's University, Kingston ON

09/10– 04/11 **Queen's University Deans Honour List with Distinction**
(90%+ average)
Queen's University, Kingston ON

09/07 – 04/10 **Queen's University Deans Honour List**
(80%+ average)
Queen's University, Kingston ON

09/07 – 04/11 **Imperial Oil Higher Education Award**
Imperial Oil, Calgary AB

09/07 – 04/11 **BP Canada Energy Academic Scholarship**
BP Canada, Calgary AB

09/07 **Queen's University Entrance Scholarship**
Queen's University, Kingston ON